Cellular/Molecular

Dynein Is Required for Rab7-Dependent Endosome Maturation, Retrograde Dendritic Transport, and Degradation

Chan Choo Yap,[1] Laura Digilio,[1] Lloyd P. McMahon,[1] Tuanlao Wang,[2] and Bettina Winckler[1]
[1]Department of Cell Biology, University of Virginia, Charlottesville, Virginia 22908, and [2]School of Pharmaceutical Sciences, Xiamen University, Xiamen, Fujian Province 361005, China

In all cell types, endocytosed cargo is transported along a set of endosomal compartments, which are linked maturationally from early endosomes (EEs) via late endosomes (LEs) to lysosomes. Lysosomes are critical for degradation of proteins that enter through endocytic as well as autophagic pathways. Rab7 is the master regulator of early-to-late endosome maturation, motility, and fusion with lysosomes. We previously showed that most degradative lysosomes are localized in the soma and in the first 25 μm of the dendrite and that bulk degradation of dendritic membrane proteins occurs in/near the soma. Dendritic late endosomes therefore move retrogradely in a Rab7-dependent manner for fusion with somatic lysosomes. We now used cultured E18 rat hippocampal neurons of both sexes to determine which microtubule motor is responsible for degradative flux of late endosomes. Based on multiple approaches (inhibiting dynein/dynactin itself or inhibiting dynein recruitment to endosomes by expressing the C-terminus of the Rab7 effector, RILP), we now demonstrate that net retrograde flux of late endosomes in dendrites is supported by dynein. Inhibition of dynein also delays maturation of somatic endosomes, as evidenced by excessive accumulation of Rab7. In addition, degradation of dendritic cargos is inhibited. Our results also suggest that GDP-GTP cycling of Rab7 appears necessary not only for endosomal maturation but also for fusion with lysosomes subsequent to arrival in the soma. In conclusion, Rab7-dependent dynein/dynactin recruitment to dendritic endosomes plays multifaceted roles in dendritic endosome maturation as well as retrograde transport of late endosomes to sustain normal degradative flux.

Key words: **degradation; dendrite; dynein; lysosome; Rab7; RILP**

Significance Statement

Lysosomes are critical for degradation of membrane and extracellular proteins that enter through endocytosis. Lysosomes are also the endpoint of autophagy and thus responsible for protein and organelle homeostasis. Endosomal-lysosomal dysfunction is linked to neurodegeneration and aging. We identify roles in dendrites for two proteins with links to human diseases, Rab7 and dynein. Our previous work identified a process that requires directional retrograde transport in dendrites, namely, efficient degradation of short-lived membrane proteins. Based on multiple approaches, we demonstrate that Rab7-dependent recruitment of dynein motors supports net retrograde transport to lysosomes and is needed for endosome maturation. Our data also suggest that GDP-GTP cycling of Rab7 is required for fusion with lysosomes and degradation, subsequent to arrival in the soma.

Introduction

Lysosomes perform degradation of membrane and extracellular proteins that enter through endocytosis (Luzio et al., 2009; Klumperman and Raposo, 2014; Marques and Saftig, 2019) or autophagy (Nixon and Yang, 2011; Kulkarni and Maday, 2018; Stavoe and Holzbaur, 2019; Farfel-Becker et al., 2020) and thus maintain protein and organelle homeostasis. Degradation requires regulated maturation of early endosomes (EEs) to late endosomes (LEs) to ensure transport of cargos to lysosomes (Huotari and Helenius, 2011; Scott et al., 2014; Naslavsky and Caplan, 2018). Rab7 is a master regulator of EE-LE maturation

Received Dec. 23, 2021; revised Mar. 30, 2022; accepted Apr. 15, 2022.
Author contributions: C.C.Y. and B.W. designed research; C.C.Y., L.D., and L.P.M. performed research; C.C.Y., L.D., and L.P.M. analyzed data; C.C.Y., L.D., and L.P.M. edited the paper; T.W. contributed unpublished reagents/analytic tools; B.W. wrote the first draft of the paper.
This work was supported by National Institutes of Health Grant R01NS083378 to B.W. We thank Dr. Kevin Pfister (University of Virginia) for reagents and advice; and Ashley Mason and Ryan Mulligan for critical reading of the manuscript.
The authors declare no competing financial interests.
Correspondence should be addressed to Bettina Winckler at bwinckler@virginia.edu or Chan Choo Yap at cy5x@virginia.edu.
https://doi.org/10.1523/JNEUROSCI.2530-21.2022

and dynamics (Vitelli et al., 1997; Bucci et al., 2000; Guerra and Bucci, 2016). Mutations in Rab7 cause Charcot-Marie-Tooth disease2B, which primarily manifests as degeneration of the longest axons (Cogli et al., 2009; Tanabe et al., 2018). Endosomal-lysosomal dysfunction is thus linked to neurodegeneration and aging (Ferguson, 2018; Jin et al., 2018a; Winckler et al., 2018; Lie and Nixon, 2019; Peng et al., 2019; Parenti et al., 2021).

Given the size and complex morphology of neurons, much work aims to understand how neuronal endosomal flux and degradation are regulated (Lasiecka and Winckler, 2011; Lasiecka et al., 2014; Bentley et al., 2015; Maday and Holzbaur, 2016; Jin et al., 2018b; Yap et al., 2018; Farfel-Becker et al., 2020; Cason et al., 2021; Gowrishankar et al., 2021). In dendrites, EEs (EEA1-positive) are mostly stationary (Lasiecka et al., 2014). When Rab7 (Wang et al., 2011) is recruited and activated on maturing EEs, they convert to motile LEs (Rab7-positive). Using the short-lived dendritic transmembrane proteins NSG1/2 (Yap et al., 2017, 2018), we previously showed that bulk degradation of NSG1/2 occurs in/near the soma where the most degradative lysosomes are localized. Expression of dominant-negative Rab7 (Rab7-DN) led to accumulation of NSG1/2 in somatic and dendritic endosomes because of reduced vesicle motility and failure to degrade NSG1/2 (Yap et al., 2018). We proposed the model that LEs need to move retrogradely toward the soma in a Rab7-dependent manner for fusion with somatic lysosomes (Yap and Winckler, 2022).

Since microtubule polarity is mixed in dendrites (Baas et al., 1989; Kapitein and Hoogenraad, 2015; Yau et al., 2016; Tas et al., 2017), retrograde transport generally can be mediated by dynein (along "plus-end-out" microtubules) or by kinesins (along "minus-end-out" microtubules). For instance, both kinesin KIF5 and dynein can act as retrograde motors in dendrites (Ayloo et al., 2017; Tas et al., 2017). In addition, dynein is an anterograde motor for some cargos in dendrites (Kapitein et al., 2010; Ayloo et al., 2017). It is unknown which motors are responsible for degradative flux of Rab7-LEs to somatic lysosomes. Using inhibition of dynein/dynactin itself or of dynein recruitment to LEs, we now ask whether dynein supports net retrograde flux of LEs in dendrites. Dynein recruitment is inhibited by overexpressing the C-terminus of RILP (RILP-Ct). RILP is a Rab7 effector that binds strongly to Rab7-GTP via its C-terminus (Cantalupo et al., 2001; Wu et al., 2005; Progida et al., 2007; Lin et al., 2014; Vallee et al., 2021). This binding specificity is often used to assess activated Rab7-GTP levels in cells (Sun et al., 2009). RILP also binds to the dynein (DLIC1)/dynactin (p150glued) complex via its N-terminus (Jordens et al., 2001; Tan et al., 2011) and promotes perinuclear clustering of LEs/lysosomes in non-neuronal cells. In neurons, RILP has been implicated in retrograde axonal transport of NGF-TrkA-signaling endosomes (Rab7- and dynein-dependent) (Ye et al., 2018) and in maturation of axonal autophagosomes via binding to ATG5 and LC-3 (Rab7- and dynein-independent) (Khobrekar et al., 2020).

We find that inhibition of dynein delays degradation of dendritic cargos (NSG1/2). We also find defects in dendrite morphology when dynein is inhibited. Unexpectedly, we find that both inhibition of dynein recruitment by RILP-Ct and direct inhibition of dynein lead to over-recruitment of Rab7 to endosomes. Dynein/dynactin recruitment to LEs thus plays multifaceted roles in dendritic endosome maturation as well as retrograde transport to sustain normal degradative flux.

Materials and Methods

Reagents used are listed in Table 1.

Neuronal cultures and transfection. Neuronal cultures were prepared as described (Yap et al., 2017). In brief, the cultures were prepared from E18 rat hippocampi, as approved by the University of Virginia Animal Care and Use Committee. All experiments were performed in accordance with relevant guidelines and regulations (ACUC protocol #3422). Hippocampi from all pups in one litter were combined and thus contained male and female animals. Cells were plated on poly-L-lysine-coated coverslips and incubated with plating medium containing DMEM with 10% horse serum. For live imaging use, neurons were plated on a 35 mm glass-bottom microwell dish (MatTek). After 4 h, the plating medium was removed and replaced with serum-free medium supplemented with B27 (Thermo Fisher Scientific), and neurons were cultured for 7-10 DIV for experimental use. Transfections were conducted using Lipofectamine 2000 (Invitrogen). Neurons at DIV7-DIV8 were transfected with GFP, GFP-p150-CC1, GFP-RILP, GFP-RILP-Ct, GFP-RILP-Nt, FYCO1-Flag, or GFP-p150-CC1 with myc-RILP for 36-40 h. To investigate the effects of overexpressed proteins on NSG2 degradation, transfected neurons were incubated with cycloheximide (CHX, 20 μg/ml) for 4 h (designated T4h) or with the solvent ethanol (designated T0). For Rab7 knockdown experiments, neurons were transfected with previously validated siRNA against rat Rab7 or siControl/nontargeting RNA. Depending on the experiment, GFP plasmid vector, GFP-Rab7, or GFP-Rab7DN, or GFP-RILP was cotransfected with siRNAs at DIV5 and incubated for 6 more days. All transfection experiments were repeated in at least 2 or 3 independently derived cultures.

Live imaging. Live imaging was performed as described previously (Yap et al., 2017, 2018). In brief, neurons were transfected at DIV7-DIV8 with the following plasmid combinations: mCherry-Rab7 with GFP-RILP, GFP-RILP-Ct, GFP, GFP-p150-CC1, or GFP-DIC2C; NSG1-mcherry with GFP-RILP, GFP-RILP-Ct, GFP, GFP-p150-CC1, or GFP-DIC2C. Neurons were maintained in PhenolRed-free Neurobasal medium, and Prolong Live anti-fade (Invitrogen) was added 30 min before live imaging. For acute inhibition of cytoplasmic dynein activity, neurons were transfected with either GFP-Rab7 or NSG1-mCherry and treated with 50 μM of ciliobrevin D or DMSO 90 min before imaging. To image the motility of DQBSA in transfected neurons, neurons were incubated with 5 μg/ml of DQ-BSA overnight, followed by washing with PBS and imaged live immediately. All live imaging was performed on a 37°C heated stage in a chamber with 5% CO_2 on an inverted Zeiss LSM880 confocal microscope using a 40× water objective (LD-C Apochromat 1.2W). Neurons with healthy morphology were chosen in regions of the coverslip with minimal overlap of transfected dendrites. For GFP-RILP imaging, dendrites with remaining Rab7 compartments were selected. Many neurons had already clustered all Rab7 compartments in response to GFP-RILP, and few dendritic compartments remained to be imaged in those cells. Plasmid concentration of GFP-RILP was reduced to increase the number of neurons that could be imaged. Images from single or dual channels were acquired simultaneously with bidirectional scan-frame mode every second for 400-500 frames and with tight gate settings to reduce cross-excitation. Laser lines at 488 nm for GFP/Emerald and at 594 nm for mCherry expression were used. Live imaging for any given set of transfected constructs was repeated in at least three independent cultures. Each time, 6-9 neurons per transfected construct were imaged live.

Immunocytochemistry. Immunostaining of neurons was conducted as described (Yap et al., 2017, 2018). Neurons were fixed in 2% PFA/4% sucrose/PBS in 50% conditioned medium at room temperature for 30 min, quenched in 10 mM glycine/PBS for 10 min. After washing with PBS, cells were then blocked in 5% horse serum/1% BSA/PBS ± 0.2% Triton X-100 or 0.1% saponin for 20 min. All antibodies were diluted in 1% BSA/PBS and incubated for 1 h. Coverslips were mounted in Prolong Gold mounting medium and viewed on a Zeiss Z1-Observer with a 40× objective (EC Plan-Neofluar 40×/0.9 Pol WD = 0.41). Structured Illumination Microscopy (Zeiss Apotome) was used for most images. Images were captured with the Axiocam503 camera using Zen software (Zeiss) and processed identically in Adobe Photoshop. No nonlinear image adjustments were performed.

Lysosome labeling. LysoTracker dye (LysoTracker Red, DND-99; 1:10,000×; Thermo Fisher Scientific: #L7528) was used to live label and

Table 1. Reagents

Reagents			
	Species	Source, catalog #	RRID
Antibodies			
Cathepsin B	Goat	R&D Systems AF965	AB_2086949
Cathepsin D	Goat	R&D Systems AF1029	AB_2087094
DNER	Goat	R&D Systems AF2254	AB_355202
NSG2	Goat	Everest Biotech EB12967	AB_2571866
NSG2	Rabbit	Abcam ab189513	AB_399409
EEA1	Mouse	BD Biosciences 610456	AB_2038958
LAMP1	Mouse	Enzo Life Sciences ADI-VAM-EN001	AB_10693925
Rab7	Rabbit	Cell Signaling 9367	AB_2629474
Rab7	Rabbit	Abcam ab137029	AB_2138173
MAP2	Chicken	EnCor Biotechnology CPCA-MAP2	AB_10974087
CI-M6PR	Rabbit	Abcam ab124767	AB_398141
GM130	Mouse	BD Biosciences 610822	AB_399947
p150glued	Mouse	BD Biosciences 612708	AB_668849
DIC	Mouse	Santa Cruz Biotechnology sc-13524	AB_627268
Myc 9E10	Mouse	Santa Cruz Biotechnology sc-40	AB_259529
Flag M2	Mouse	Sigma, F3165	AB_2313564
β3-tubulin	Chicken	Aves Labs, TUJ	AB_141607
Alexa-488 anti-mouse	Donkey	Invitrogen A21202	AB_2535792
Alexa-488 anti-rabbit	Donkey	Invitrogen A21206	AB_2534102
Alexa-488 anti-goat	Donkey	Invitrogen A11055	AB_2534013
Alexa-568 anti-mouse	Donkey	Invitrogen A10037	AB_2534017
Alexa-568 anti-rabbit	Donkey	Invitrogen A10042	AB_2534104
Alexa-568 anti-goat	Donkey	Invitrogen A11057	AB_162546
Alexa-647 anti-mouse	Donkey	Invitrogen A31571	AB_2536183
Alexa-647 anti-rabbit	Donkey	Invitrogen A31573	AB_2535864
Alexa 647 anti-goat	Donkey	Invitrogen A21447	AB_2340373
Dylight 405 anti-chicken	Donkey	Jackson ImmunoResearch Laboratories 703-475-155	
Alexa 680 anti-mouse	Donkey	Jackson ImmunoResearch Laboratories 715–625-151	
Alexa 790 anti-rabbit	Donkey	Jackson ImmunoResearch Laboratories 711–655-162	
Alexa-680 anti-chicken	Donkey	Jackson ImmunoResearch Laboratories 703–625-155	
Alexa-800 anti-goat	Donkey	LICOR Biosciences 926–32214	
Plasmids			
NSG1-mcherry	Yap et al., 2017		
EGFP-Rab7	Addgene, #12605, Richard Pagano laboratory (Choudhury et al., 2002)		
EGFP-Rab7T22N	Addgene, #12660, Richard Pagano laboratory (Choudhury et al., 2002)		
mCherry-Rab7	Gift from Michael Davidson laboratory		
GFP-RILP	Wang and Hong, 2006		
GFP-RILP199-401	Wang and Hong, 2006		
GFP-RILP1-198	Wang and Hong, 2006		
Myc-RILP	Wang and Hong, 2002		
GFP-p150-CC1	Gift from Dr. Kevin Pfister		
GFP-DIC2C	Gift from Dr. Kevin Pfister		
FYCO1-Flag	Genscript clone ID: OHu21346		
GFP	Clontech		
mCherry	Clontech		
siRNA-rat Rab7	5′-GACCAAGAACACACACGUA, Dharmacon #J-089334-10-0010		
siControl-nontargeting RNA	5′-UGGUUUACAUGUCGACUAA, Dharmacon #D-001810-01-05		
Chemicals			
LysoTracker Red DND99	Thermo Fisher Scientific #L7528		
DQRedBSA	Thermo Fisher Scientific #D12051		
Ciliobrevin D	Millipore Sigma #250401		
CHX	Millipore Sigma #C7698		
DMSO	Millipore Sigma #D2650		

track acidified compartments in transfected neurons using the manufacturer's protocol. Images of LysoTracker loaded transfected neurons were captured live with the Axiocam503 camera on the AxioObserver.Z1 with a 40× objective (enhanced chemiluminescence Plan Neofluar 40×/0.9 Pol; working distance, N.A. 0.41) using Zen software and processed identically in Photoshop. Live labeling of lysosomal marker in neurons was repeated in at least three independent cultures.

Western blot. Freshly dissociated E18 rat hippocampal neurons were electroporated with GFP, GFP-RILP, or GFP-RILP-Ct using Lonza Amaxa, plated, and grown for 3 d. At DIV3, transfected neurons were washed with PBS and resuspended in Tris-SDS sample buffer for Western blot analysis.

Kymograph analysis. All kymographs were generated using the Multi Kymograph plug-in for FIJI. Kymographs were analyzed using the machine learning program Kymobutler (Jakobs et al., 2019). For training

the algorithm, 35 kymographs were manually annotated and analyzed by Kymobutler. Parameters were adjusted and specifically optimized for this dataset from our laboratory. Accurate identification of vesicle tracks by the program was confirmed visually and compared with the manually established ground truth. Optimization was repeated until track identification by Kymobutler matched the manual identification. Quantification by Kymobutler included distances traveled. Net anterograde and retrograde track distances are reported regardless of pauses or direction changes during the trajectory. Six to 9 neurons per transfected construct per experiment were analyzed for three or more independent experiments. For analysis of dually positive trajectories, a new ImageJ Plugin was developed, called KymoMerge (McMahon et al., 2021).

Quantification of NSG2 and EEA1 soma intensity. Soma intensities were quantified using Imaris 9.5.1. Briefly, the transfected cells were identified, the somata were masked, and the average intensity was measured after background correction. Between 20 and 30 cells per experiment were quantified for three independent experiments.

Quantification of p150^{glued}. p150^{glued} levels on Rab7-positive late endosomes in the soma were quantified in each cell transfected with GFP, GFP-RILP, or GFP-RILP-Ct by creating a mask for Rab7-positive pixels and then determining the average p150^{glued} staining intensity in the Rab7-positive mask using Imaris 9.3.1.

Quantification of soma clustering. Neurons transfected with GFP, GFP-RILP, GFP-RILP-Nt, or GFP-RILP-Ct were counterstained with MAP2 to identify dendrites and one of the following markers: Rab7, EEA1, GM130, LAMP1, CatB, CI-M6PR, NSG2, or DNER. Transfected cells were scored as to whether the staining was changed in the transfected cells compared with nearby untransfected cells. Markers scored as "nonclustering" in transfected cells cannot be distinguished from untransfected cells by a blinded observer.

Quantification of intensity and density of endosomal compartments in dendrites. Because of the extensive crisscrossing of dendrites from different neurons in the field of view, it is difficult to determine the total NSG2 fluorescence in dendrites. We therefore determined both the average NSG2 intensity/endosome and the number of NSG2-positive endosomes per unit length of dendrite using the "Spot" function of Imaris to identify individual endosomes. Transfected cells were identified, and dendrites were masked using Imaris 9.3.1. Spot objects were created for labeled markers within the dendrite mask. The average intensity of all puncta per cell was tabulated. Data were normalized to the GFP control and combined from three independent experiments. For the density calculation, the number of puncta per dendrite area per cell was tabulated and combined from three independent experiments. Ten to 15 cells with 1-10 dendrites/cell per experiment were counted.

Measurement of dendrite length. All dendrites on each transfected cell were traced and lengths measured using Filament Tracer in Imaris 9.5.1. Total length per cell is reported for 20 cells/condition/experiment from three independent experiments. Scholl calculations were done within Imaris using the same filament tracings.

Quantification of Rab7 compartment intensity and size. Because of diffuse fluorescence due to cytosolic Rab7, object-based analysis was done for Rab7. Somata of transfected cells were masked using Imaris 9.5.1. Within the masked regions, surfaces representing Rab7 compartments were created. The number and average fluorescence intensity of compartments >2 μm^2 were reported. $N = 30$ cells from three separate experiments were analyzed.

Experimental design and statistical analyses. All experiments were performed with all conditions in parallel in the same cultures at the same time. This includes live imaging of all plasmid combinations for any given experiment on the same day. Therefore, different plasmid transfections can be compared with more confidence since culture-to-culture variation would affect all experimental conditions equally on any given day. This experimental design minimizes contributions of culture-to-culture variability to the observed differences.

All experiments were repeated several times in independent cultures, as indicated in the figure legends. Exclusion of dendrites from analysis had to meet predetermined criteria. The most common reason for exclusion was crowdedness and criss-crossing of transfected and untransfected dendrites, making correct assignment of puncta to the transfected cell ambiguous. All dendrites on all cells were thus included in the analysis unless one of two exclusion criteria was met: (1) the dendrite was shorter than 10 μm, or (2) extensive crisscrossing by other transfected processes obscured the kymograph making it unscoreable; ~5% of dendrites met exclusion criteria.

All data were analyzed using Prism software version 9.5.1. Each dataset was first evaluated for normality by using the Shapiro–Wilk normality test. The result was used to determine whether parametric or nonparametric tests were used. When more than one comparison was made, the corresponding ANOVA test was used. When only two conditions were compared, a *t* test was used. All *N* values are shown in the figure legends.

Results

Overexpression of a dynein adaptor causes somatic clustering of Rab7-positive late endosomes

Rab7 interacts with a large number of Rab7 effectors, which associate preferentially with the activated GTP-bound Rab7 while bound to endosomes (Guerra and Bucci, 2016; Langemeyer et al., 2018; Stroupe, 2018; Borchers et al., 2021). Inactive, GDP-bound Rab7 does not bind these effectors and dissociates from endosomes to a cytosolic pool. Among Rab7 effectors are proteins that recruit microtubule motors to Rab7-positive compartments (Cantalupo et al., 2001; Jordens et al., 2001; Johansson et al., 2007; Pankiv et al., 2010; Tan et al., 2011). In order to ask whether dynein or kinesin were the retrograde motor for Rab7-positive LEs in dendrites, we overexpressed two different Rab7 effectors that serve as motor adaptors: RILP, which links Rab7 LEs to dynein; and FYCO1, which links Rab7 LEs to kinesin. We find that overexpressed FYCO1 associated efficiently with dispersed compartments that accumulated Rab7 but did not cause somatic clustering of Rab7 (Fig. 1*A*,*D*). RILP overexpression, on the other hand, led to massive relocalization of RILP-positive Rab7 LEs to the soma (Fig. 1*B*,*D*), with only occasional LEs left in dendrites and most LEs in a single, tight perinuclear cluster. A neuron transfected with GFP is shown in Figure 1*C*. Consistent with the known role of RILP as a Rab7 effector, downregulation of Rab7 with siRab7 prevented recruitment of GFP-RILP to endosomal compartments resulting in diffuse cytosolic localization of GFP-RILP instead (Fig. 1*E*, middle). RILP-induced somatic clustering of LEs thus depends on Rab7. Unexpectedly, RILP overexpression also resulted in greatly increased Rab7 signal (compare untransfected and transfected Rab7 signals in Fig. 1*B*; also compare to GFP panel in Fig. 1*C*). Increased Rab7 in response to RILP overexpression was not observed in previous work using Mel JuSo cells (Jordens et al., 2001) but is striking in our neuronal cultures (see below for more analysis).

Rab7-negative compartments are not clustered by RILP overexpression

Next, we analyzed the effects of RILP overexpression on Rab7-negative compartments, such as the Golgi and EEs. We included two controls, namely, the N-terminal and C-terminal halves of RILP. RILP-Nt binds to dynein/dynactin but not Rab7, whereas RILP-Ct binds to Rab7 but not dynein/dynactin motor complex (Cantalupo et al., 2001) (Fig. 2*A*). In control neurons expressing GFP, Rab7-positive LEs and EEA1-positive EEs are found mostly dispersed throughout the soma and dendrites (Fig. 2*B*, arrow) with occasional higher density of compartments in the perinuclear region. Overexpression of GFP-RILP (Fig. 2*C*), but not of GFP-RILP-Ct (Fig. 2*D*,*F*, green bar), caused tight clustering of Rab7 in the soma. Similarly, overexpression of GFP-RILP-Nt did

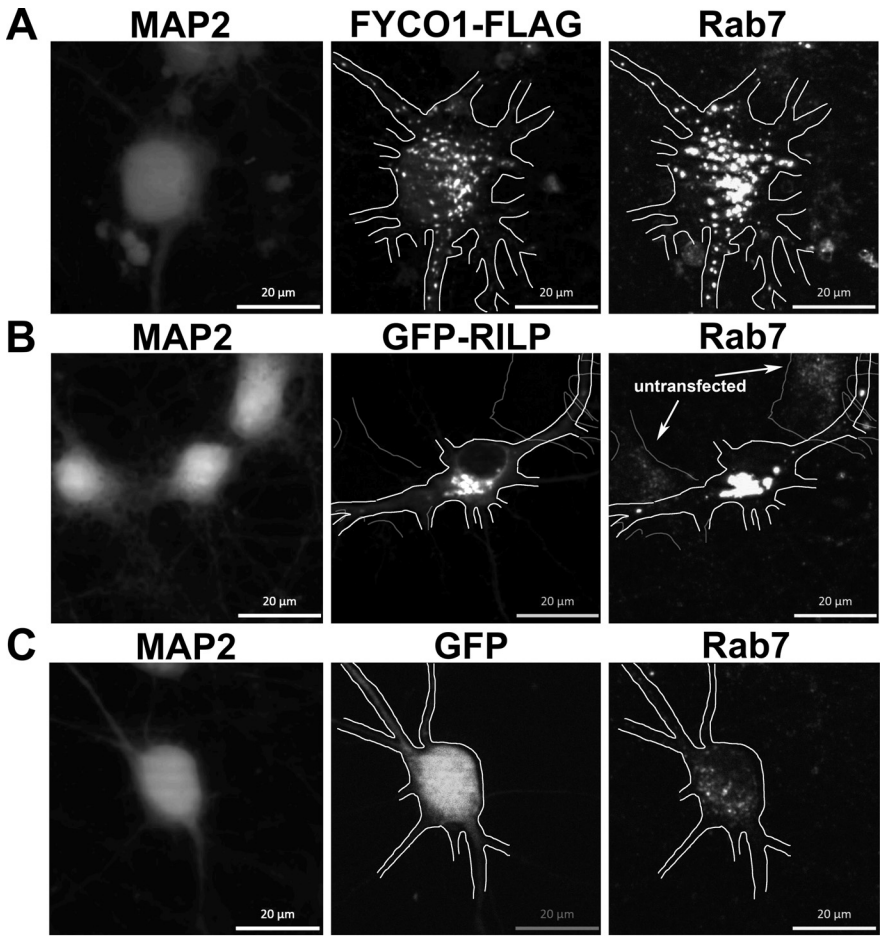

D

Rab7 distribution	transfected with GFP	WT RILP	WT FYCO1
	(# of cells from two experiments)		
same as untransfected: dispersed	166	6	0
tight cluster in soma, absent from dendrites	10	190	1
accumulated in dispersed compartments	0	0	107

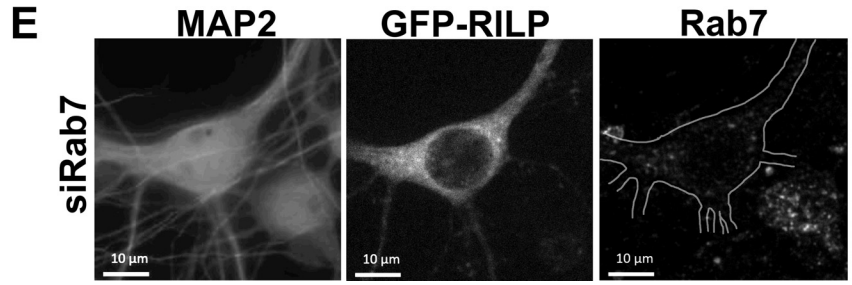

Figure 1. Overexpression of a dynein adaptor, RILP, but not of a kinesin adaptor, FYCO1, causes somatic clustering of Rab7-positive late endosomes. ***A-C***, DIV8 neurons were transfected with FYCO1-FLAG (***A***), GFP-RILP (***B***), or GFP (***C***). Cells were stained against the respective tags (middle panels) as well as against endogenous Rab7 (right panels). Left panels, MAP2 staining. The transfected neuron is outlined in each case. ***D***, Quantification of distribution patterns of endogenous Rab7 in neurons transfected with GFP, GFP-RILPWT, or FYCO1-FLAG. The distribution was scored as "clustered" if Rab7 localized to a single perinuclear site in the soma. The majority of neurons expressing RILP-WT showed tight somatic clustering of Rab7, whereas FYCO1 overexpression resulted in dispersed Rab7 throughout the soma and dendrites. $N = 108$-196 neurons from two independent cultures. ***E***, Neurons transfected for 6 d with siRab7 together with GFP-RILP (middle) were stained against MAP2 (left) and endogenous Rab7 (right). Depletion of Rab7 led to cytosolic GFP-RILP in the transfected cell (outlined), indicating that Rab7 is required for clustering of RILP in the soma.

not cluster Rab7 (Fig. 2*E*,*F*, purple bar). We note that GFP-RILP-Ct led to higher Rab7 intensity on GFP-RILP-Ct-positive compartments (see also below), but these compartments were still dispersed throughout the soma as well as along dendrites. EEs (detected with EEA1; right hand panels), on the other hand, were not affected (Fig. 2*F*). The Golgi (detected with GM130) was also not affected in its distribution by GFP-RILP overexpression (Fig. 2*F*), consistent with RILP being recruited specifically to Rab7-positive compartments.

Overexpression of the dynein adaptor RILP causes somatic clustering of lysosomes

Rab7 is found on multiple compartments along dendrites which can be distinguished by the presence of LAMP1. "Early LEs" are Rab7-positive but LAMP1-negative, whereas "late LEs" are Rab7-positive and LAMP1-positive (Yap et al., 2018). In contrast to LEs, lysosomes contain high levels of cathepsins in addition to LAMP1. Most Rab7 compartments in the soma and in the first 25 µm of the dendrite are late LEs (low degradative capacity) as well as lysosomes (highly degradative). We determined whether lysosomes were also clustered in the soma by RILP overexpression. Lysosomes were identified as dually positive LAMP1/cathepsin compartments (Fig. 3). Overexpression of GFP-RILP (Fig. 3*B*,*B*′,*E*, black bars) caused extensive somatic clustering of both LAMP1 and CatB, compared with GFP alone (Fig. 3*A*,*A*′,*E*, white bars). Deletion of the dynein/dynactin binding site (GFP-RILP-Ct) (Fig. 3*D*,*D*′,*E*, green bars) or the Rab7 binding site (GFP-RILP-Nt; Fig. 3*C*, *C*′,*E*, purple bars) prevented clustering of either LAMP1 or CatB (Fig. 3*E*). In addition, we determined the distribution of acidified compartments using live imaging of LysotrackerRed and found that acidified compartments are also clustered by GFP-RILP but not by RILP-Ct or RILP-Nt (Fig. 3*E*). We thus conclude that LEs and lysosomes are relocated into tight perinuclear clusters by overexpression of RILP in a manner that depends on the ability of RILP to bind dynein/dynactin and Rab7.

We then determined whether short-lived membrane receptors which are rapidly transported to the lysosome are also clustered by overexpressed GFP-RILP. We used two short-lived dendritic receptors, NSG2 and DNER (Yap et al., 2017, 2018). We find that both DNER (Fig. 4*B*) and NSG2 (Fig. 4*C*) are co-clustered by GFP-RILP, but not GFP-RILP-Ct or GFP-RILP-Nt (Fig. 4*D*). M6PR, in contrast, which is not short-lived and cycles between

the TGN and endosomes, does not alter its distribution when GFP-RILP is overexpressed (Fig. 4*A*,*D*).

Somatic clustering of LEs by RILP overexpression requires dynein function

We next tested whether RILP required dynein function to cause somatic clustering of LEs/lysosomes. We first determined whether endogenous localization of the dynactin subunit p150^{glued} was affected by overexpression of GFP-RILP (Fig. 5). Overexpression of GFP-RILP caused co-clustering of endogenous p150^{glued} (Fig. 5*A*) together with endogenous Rab7. GFP-RILP-Ct, which is not able to bind to the dynein motor complex, in contrast, did not affect the localization of endogenous p150^{glued} (Fig. 5*B*). When we quantified the levels of p150^{glued} on Rab7 LEs, we find a 1.5-fold enrichment when GFP-RILP is overexpressed (Fig. 5*C*), suggesting that the increased RILP levels on Rab7 LEs lead to excess recruitment of both Rab7 and p150^{glued}. Similarly to p150^{glued}, endogenous dynein intermediate chain (DIC) was co-clustered with GFP-RILP but not with GFP-RILP-Ct (Extended Data Fig. 5-1).

We then asked whether RILP overexpression still led to somatic clustering of Rab7 if dynein motor function was inhibited. We used the dominant-negative CC1 construct to inhibit dynactin/dynein function. CC1 consists of the first coiled coil domain of p150^{glued} (Quintyne et al., 1999). Its overexpression prevents assembly of the dynein/dynactin complex and potently inhibits dynein motor function. GFP-CC1 coexpression prevented somatic clustering of myc-RILP (Fig. 5*D*). Endogenous Rab7 similarly failed to be clustered in the soma, but it was still recruited to endosomes where it colocalized with the dispersed myc-RILP (Fig. 5*D*). We conclude that enhancing the recruitment of dynein onto LEs using RILP overexpression changes their steady-state distribution and clusters them in the soma. We hypothesize that dynein mediates net retrograde movement of LEs along dendrites to the perinuclear region of the soma.

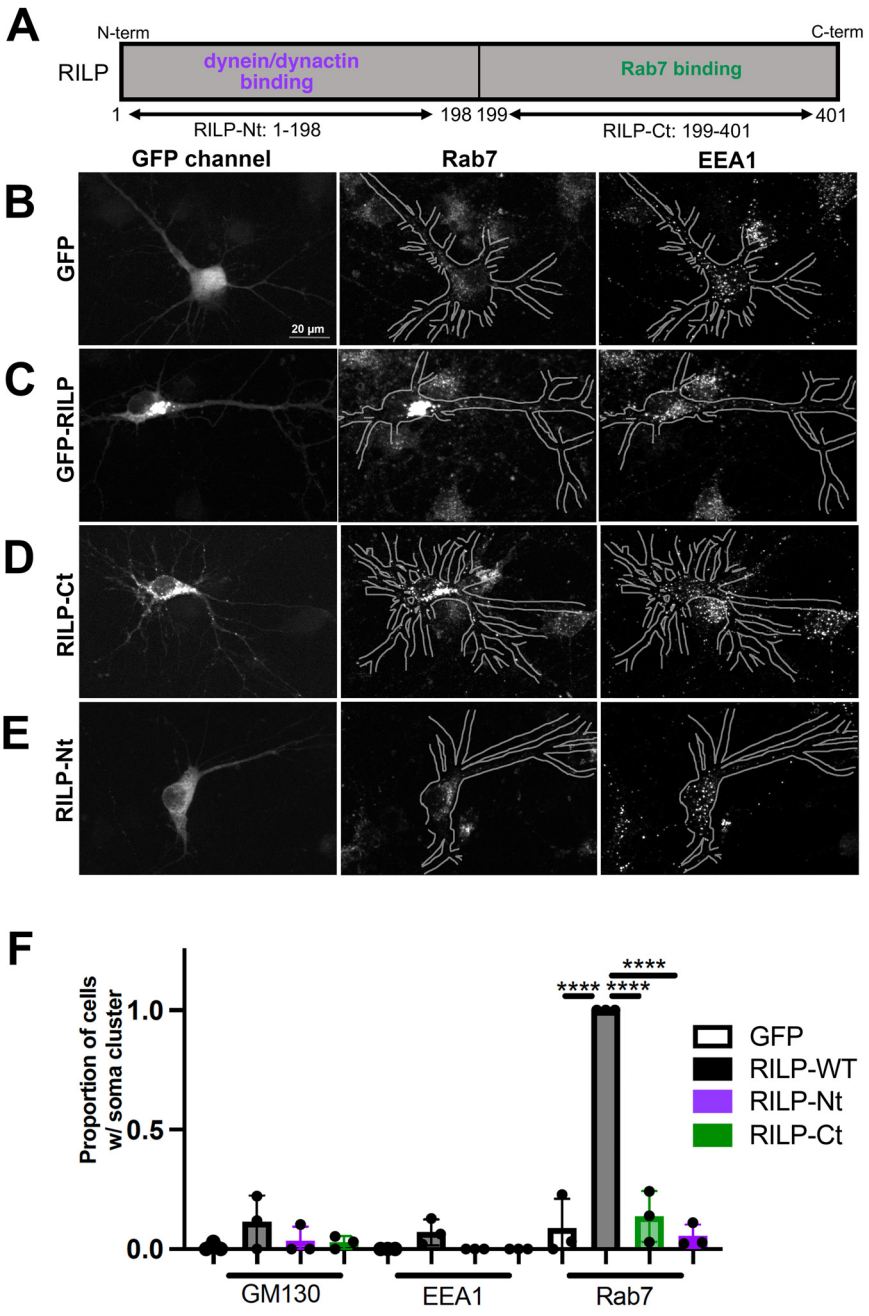

Figure 2. Rab7-negative compartments are not clustered by RILP overexpression. ***A***, Diagram of RILP showing the dynein/dynactin complex binding region (1-198) at the N-terminus and the Rab7 binding region (199-401) at the C-terminus. ***B-E***, DIV8 neurons were transfected with either GFP (***B***), GFP-RILP (***C***), GFP-RILP-Ct (***D***), or GFP-RILP-Nt (***E***) and stained against endogenous Rab7 (middle) and EEA1 (right). RILP overexpression (***C***) caused a single tight cluster of Rab7 in the soma, whereas RILP-Ct overexpression (***D***) led to increased Rab7 dispersed in the soma and along the dendrites. RILP-Nt did not change Rab7 levels or distribution. Overexpression of RILP, RILP-Ct, or RILP-Nt did not alter the distribution of the early endosome marker, EEA1. Transfected neurons are outlined. Staining of untransfected neurons in the same field is also visible. ***F***, Quantification of the proportion of neurons showing a single, tight somatic cluster of marker proteins in neurons transfected with either GFP (white bar), GFP-RILP (black bar), GFP-RILP-Nt (purple bar), or GFP-RILP-Ct (green bar). EEA1 is a marker for early endosome, Rab7 for late endosome, and GM130 for Golgi. $N = 3$ independent cultures (61-124 neurons quantified in three experiments). ****$p < 0.0001$ (ANOVA with Tukey's multiple comparisons test). Errors bars show standard deviations.

Motility of dendritic LEs is affected by overexpression of WT RILP or RILP-Ct

We next tested whether recruiting dynein to LEs by overexpressing RILP or preventing recruitment of dynein by overexpressing RILP-Ct changed dendritic motility of LEs (marked by mCherry-Rab7). We conducted live imaging in dendrites of neurons transfected with mCh-Rab7 together with GFP, GFP-RILP, or GFP-RILP-Ct (Fig. 6). As we and others reported previously (Schwenk et al., 2014; Yap et al., 2018; Boecker et al., 2020), Rab7 compartments in dendrites move in both anterograde and retrograde directions with many pauses and reversals of direction (Fig. 6*A*). In order to evaluate net motility

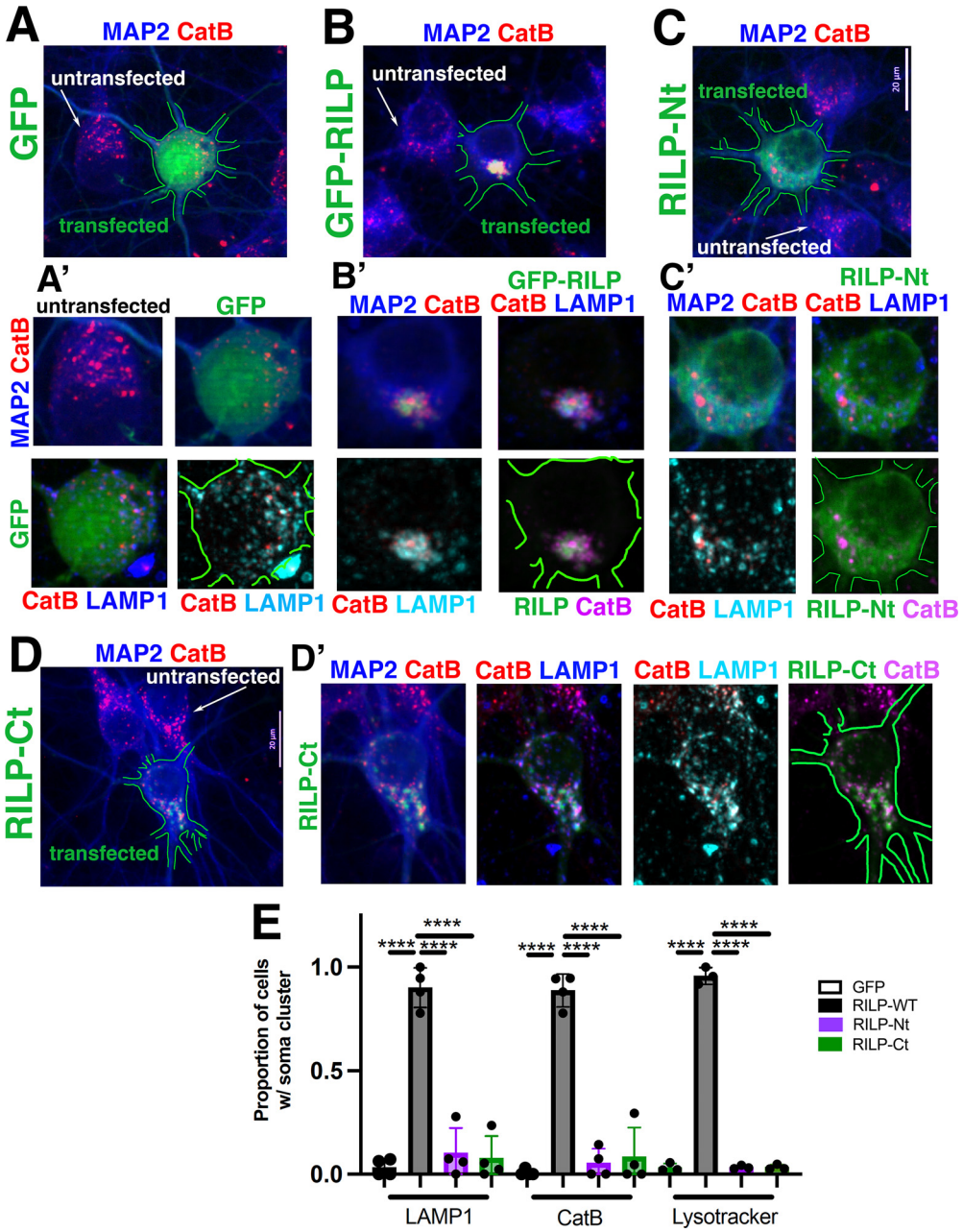

Figure 3. Overexpression of the dynein adaptor RILP causes somatic co-clustering of lysosomes. ***A-D***, DIV8 neurons were transfected with GFP (***A***), GFP-RILP (***B***), GFP-RILP-Nt (***C***), or GFP-RILP-Ct (***D***) and stained against endogenous MAP2 (blue), CatB (red), and LAMP1 (shown in ***A′-D′***). Transfected neurons are outlined in green. White arrows indicate untransfected neurons. GFP-RILP overexpression caused tight clustering of CatB in the perinuclear region of the soma, whereas RILP-Ct overexpression led to dispersed distribution of CatB, similar to GFP expression. Neurons transfected with GFP or RILP-Nt were indistinguishable from untransfected neurons. ***A′-C′***, Magnified images of transfected soma. Similarly to CatB, LAMP1 (turquoise/blue) also tightly clustered in the perinuclear region of the soma of the neuron expressing GFP-RILP (***B′***). ***E***, Quantification of the frequency of somatic clustering of lysosomal compartments labeled with CatB, LAMP1, or LysotrackerRed, in neurons transfected with GFP (white bar), GFP-RILP (black bar), GFP-RILP-Nt (purple bar), or GFP-RILP-Ct (green bar). $N = 3$ or 4 independent experiments (97-213 neurons quantified in 3 or 4 experiments). $^{****}p < 0.0001$ (ANOVA with Tukey's multiple comparisons test). Error bars correspond to standard deviations.

regardless of intermittent pauses or reversals, we determined the net movement of each vesicle trajectory in ~500 s of live imaging. Net movements of trajectories were quantified for all dendrites of each recorded neuron. Figure 6*B* shows the proportions of dendrite trajectories per cell which undergo no net movement (purple bar), small (<2 µm) net movements in either the anterograde (gray) or retrograde (blue) directions, or large (≥2 µm) net movements in either the anterograde (pink) or retrograde (green) directions. The actual net distances which were combined into the pink, gray, blue, and green portions of the bar graph are shown in Extended Data Figure 6-1. The proportion of total retrograde versus anterograde or of long distance (≥2 µm) retrograde versus anterograde trajectories is shown in Figure 6*E*. Net motility of mCh-Rab7 is not biased directionally in a 500 s imaging window. Interestingly, overexpression of WT GFP-RILP leads to a statistically significant increase in the retrogradely long distance (≥2 µm) proportion (Fig. 6*B*, green bars; Fig. 6*E*) compared with GFP controls. In contrast, overexpression of GFP-RILP-Ct increases the stationary population (Fig. 6*B*, purple bar) and decreases both anterograde and retrograde populations (Fig. 6*B*, pink and green bars). No changes were observed in the proportion of short

distance (<2 µm) net displacements in either direction (Fig. 6*B*, gray and blue bars). The biggest effects are thus observed for long range (≥2 µm) net movements of Rab7 compartments.

Since not all Rab7$^+$ LEs are positive for GFP-RILP (~70%), we specifically analyzed the motility of Rab7 compartments which also contained GFP-RILP ("dual Rab7$^+$/RILP$^+$") (Fig. 6*C*,*D*). We used a newly developed plugin for ImageJ/Fiji, called KymoMerge, to create kymographs of dually positive trajectories (McMahon et al., 2021). Analysis of dually positive (Rab7$^+$/RILP$^+$) compartments showed statistically significantly higher retrograde versus anterograde motility (Fig. 6*E*), something we did not consistently observe for total mCh-Rab7. When considering the proportion of net retrograde versus net anterograde trajectories (distances >0), we find a small retrograde bias for dually positive Rab7$^+$/RILP$^+$ compartments which closely matches the slight excess of plus-end out microtubules in dendrites (55% plus-end out) (Fig. 6*E*). If only the longer (≥2 µm) net trajectories of dually positive Rab7$^+$/RILP$^+$ compartments are analyzed, the retrograde bias increases to 62:38 (Fig. 6*D*, green vs pink bars; Fig. 6*E*). Net distances traveled are shown in Extended Data Figure 6-1. If the total distances for anterograde and retrograde transport of dually positive Rab7$^+$/RILP$^+$ compartments are summed, we find that 64% of the absolute net displacement is in the retrograde direction (2113 µm retrograde displacement/3395 µm total distance). These observations suggest that RILP-mediated recruitment of dynein increases the proportion of motile compartments at the expense of stationary populations. This effect appears biased in the retrograde direction.

When dynein recruitment to Rab7 compartments is inhibited by overexpression of GFP-RILP-Ct, bidirectional motility of dually positive compartments is inhibited (Fig. 6*D*). As we observed for total mCh-Rab7 populations as well (Fig. 6*B*), the short-range populations (<2 µm; gray and blue bars) are unaffected (Fig. 6*D*). Uncoupling LEs from dynein motors using RILP-Ct thus impairs bidirectional long-range motility (≥2 µm) but has little or no effect on short net excursions (<2 µm).

siRab7 delays degradation of a short-lived dendritic cargo

We previously showed that expression of the dominant-negative Rab7T22N blocked degradation of NSG2 (Yap et al., 2018). In order to monitor degradation, we block

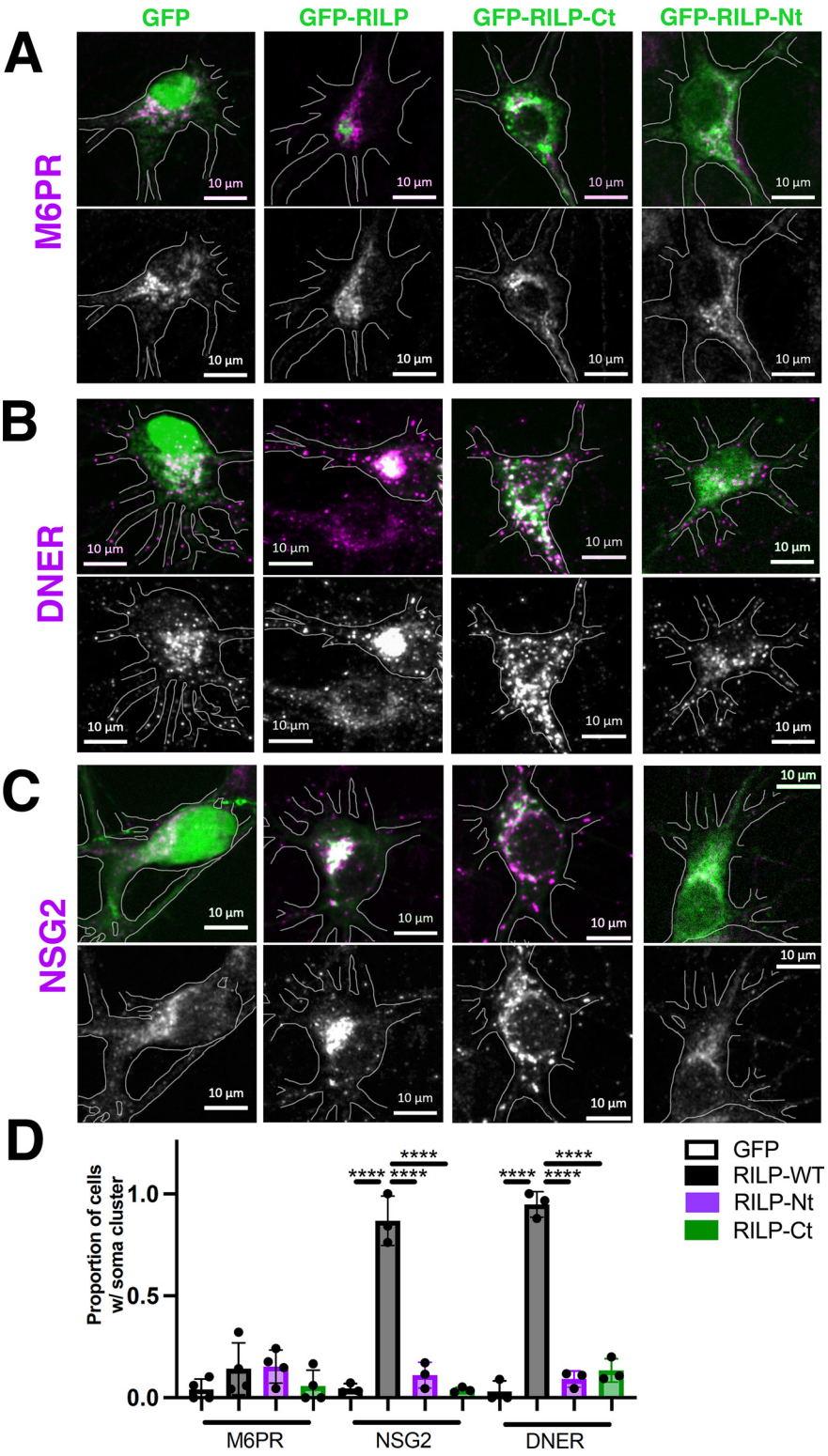

Figure 4. Overexpression of the dynein adaptor RILP causes somatic co-clustering of degradative cargo-containing compartments. ***A-C***, DIV8 neurons were transfected with GFP, GFP-RILP, GFP-RILP-Ct, or GFP-RILP-Nt and stained against MAP2 and endogenous M6PR (***A***), DNER (***B***), or NSG2 (***C***). Transfected neurons are outlined in white based on MAP2 staining, which is not shown. The marker channel alone is shown in the bottom row. ***D***, Quantification of the frequency of somatic clustering of cargo-containing compartments labeled by M6PR, or short-lived cargos, NSG2 and DNER, in neurons transfected with GFP (white bar), GFP-RILP (black bar), GFP-RILP-Nt (purple bar), or GFP-RILP-Ct (green bar). $N = 3$ or 4 independent experiments (83-111 neurons quantified in 3 or 4 experiments). ****$p < 0.0001$ (ANOVA with Tukey's multiple comparisons test). Error bars correspond to standard deviations.

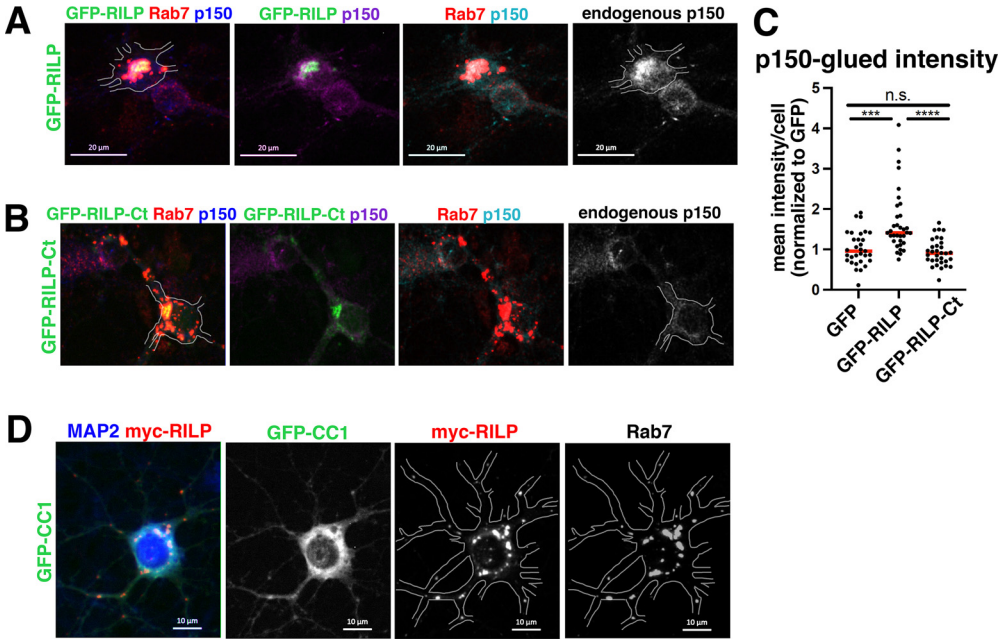

Figure 5. Somatic clustering of LEs by RILP co-clusters dynein/dynactin and requires dynein function. DIV8 neurons were transfected with GFP-RILP (***A***) or GFP-RILP-Ct (***B***) and stained against endogenous Rab7 and p150-glued. ***A***, Endogenous p150glued (blue/magenta/cyan as labeled) accumulated and colocalized with GFP-RILP and endogenous Rab7 (red) in neurons expressing GFP-RILP. In contrast, overexpression of RILP-Ct (***B***) did not alter the distribution of p150glued. Transfected neurons are outlined based on MAP2 staining. Gray represents single channels of p150glued. ***C***, The level of p150glued present on Rab7-positive endosomes per cell was quantified and normalized to GFP control neurons. $N = 31$ cells (GFP), 34 cells (GFP-RILP), 32 cells (GFP-RILP-Ct) were quantified from three independent experiments. ***$p < 0.001$; ****$p < 0.0001$; Kruskal–Wallis with Dunn's multiple comparisons test. Extended Data are included in Extended Data Figure 5-1, showing staining against DIC. ***D***, DIV8 neurons were cotransfected with GFP-CC1 (to inhibit dynein) and myc-RILP and stained against endogenous Rab7. Transfected neuron is outlined. Gray represents single channels. Overexpression of GFP-CC1 prevented somatic clustering of myc-RILP.

new translation with CHX for 4 h and determine levels of NSG2. Steady state (designated "T0") corresponds to control cultures treated with ethanol, the solvent for CHX (Yap et al., 2018). We wondered how loss of Rab7 function compared with preventing dynein recruitment to LEs in terms of degradation of short-lived dendritic cargos (e.g., NSG2). In order to assess degradation blocks comparatively across various conditions, we decided to first establish a baseline using downregulation of Rab7 by siRNA. Unlike Rab7T22N overexpression, siRab7 allows us to perform rescue experiments for more rigorous controls. siRab7 efficiency was evaluated in cultured rat hippocampal neurons 6 d after transfection of dissociated E18 rat hippocampal neurons (DIV5-DIV11). Rab7 levels were significantly diminished in siRab7-treated cultured rat hippocampal neurons to ~50% of control levels (siCon) ($n = 3$ experiments; ± 4% SD) (Fig. 7*Aa*,*Ab*). The quantification is shown in Extended Data Figure 7-1. This is in line with our experience of other knockdown efficiencies (Lasiecka et al., 2010; Yap et al., 2012).

Similarly to expression of Rab7-DN, downregulation of Rab7 with siRab7 resulted in accumulation of NSG2 (Fig. 7*C*,*E*) compared with siCon (~2.2-fold) (Fig. 7*B*,*E*). Cotransfection of siRab7 with GFP-Rab7 (Fig. 7*D*,*E*), but not with Rab7-DN (Fig. 7*E*), rescued NSG2 levels back down to control levels, consistent with an on-target effect of siRab7. Next, we conducted a CHX chase experiment for 4 h, as before. In control cultures (siCon), NSG2 was efficiently cleared and only ~35% of NSG2 signal remained in the soma after 4 h in CHX (Fig. 7*F*). Somatic clearance of NSG2 was significantly slowed in siRab7 (~60% remaining) compared with siCon but was not completely blocked. This could be because of the partial downregulation of Rab7 achieved by siRab7. The degradation defect could be rescued with coexpression of WT GFP-Rab7 but not GFP-Rab7-DN (Fig. 7*F*).

In addition to accumulation of NSG2 in the soma (Fig. 7*B* vs Fig. 7*C*; Fig. 7*E*), we also observed accumulation along dendrites (Fig. 7*B*′,*C*′). Accumulated NSG2 in dendrites was found in very bright endosomes which often appeared clustered and/or enlarged. NSG2 intensity per endosome increased ~3-fold in dendrites in siRab7 (Fig. 7*G*) compared with siCon, whereas the density of compartments did not change in siRab7 (Fig. 7*H*). After 4 h in CHX (Fig. 7*H*), the density of NSG2 compartments along dendrites was reduced ~4-fold in siCon. This observation is consistent with the notion that NSG2 is transported toward the soma during the chase time in CHX. SiRab7 led to a significant increase in NSG2 intensity in dendritic endosomes in controls (T0 = no CHX) which did not decline in the CHX chase (CHX 4 h) (Fig. 7*G*). Similarly, dendrite density was much more reduced after 4 h in CHX in siCon compared with siRab7 (Fig. 7*H*), indicating accumulation of NSG2 in dendritic compartments which fail to reach lysosomes.

Preventing dynein recruitment to LEs leads to degradative delays

We next wondered whether preventing dynein recruitment to Rab7 compartments by overexpression of RILP-Ct affected degradation of short-lived dendritic cargos (e.g., NSG2). Soma levels of NSG2 were quantified in neuron cultures transfected with GFP (Fig. 8*A*,*D*), GFP-RILP (Fig. 8*B*,*D*), or GFP-RILP-Ct (Fig. 8*C*,*D*) at steady state (no CHX = T0; Fig. 8*E*) or 4 h after CHX addition (T4h) (Fig. 8*F*). At T0, NSG2 levels were elevated significantly in GFP-RILP-Ct-expressing neurons compared with GFP controls (Fig. 8*D*,*E*). Chasing for 4 h after translation block in CHX additionally indicated that GFP-RILP-Ct significantly impaired NSG2 degradation (Fig. 8*F*), almost to the same degree as siRab7. The same phenotype was observed for GFP-RILP-Ct in dendrites (compare line scans in Fig. 8*A*′,*C*′) where NSG2

accumulated all along dendrites (Fig. 8*C′*). We note that NSG2 in dendrites was often found in bunches of clustered enlarged endosomes which were not evenly dispersed, similarly to our observations in siRab7 (Fig. 7). We conclude that failure to recruit dynein to LEs leads to accumulation of NSG2 in clusters of endosomes dispersed along dendrites and impairment in degradation of the short-lived dendritic cargo NSG2. Interestingly, overexpression of full-length GFP-RILP also resulted in NSG2 accumulation at T0 (Fig. 8*D*,*E*). Degradation of NSG2 after 4 h CHX was also impaired by GFP-RILP overexpression (Fig. 8*F*), albeit to a somewhat lesser degree than RILP-Ct.

Motility of NSG1 is impaired by RILP-Ct

Since overexpression of RILP-Ct results in accumulation of NSG2 in enlarged/clustered endosomes along dendrites and in reduction of NSG2 degradation, we next conducted live imaging of vesicles transporting degradative cargos. GFP, GFP-RILP, or GFP-RILP-Ct was overexpressed together with NSG1-mCh (Fig. 8*G*,*H*) and imaged live (as in Fig. 6). Our previous experiments established that ~60% of NSG1 compartments are colocalized with Rab7 (Yap et al., 2017). NSG1-mCh compartments displayed bidirectional motility (Fig. 8*G*), reminiscent of Rab7 LEs. Transport direction was slightly but significantly skewed toward retrograde (57% retrograde, pink vs green bars; Fig. 8*H*, red star). Overexpression of GFP-RILP did not change NSG1-mCh motility significantly (Fig. 8*H*). In contrast, overexpression of GFP-RILP-Ct significantly decreased motility of NSG1-mCh in both directions (Fig. 8*G*,*H*; Extended Data Fig. 8-1). We conclude that failure to recruit dynein to LEs leads to reduction in net retrograde motility (for both Rab7 itself and the short-lived cargo NSG1), accumulation of degradative cargos in dispersed endosomes along dendrites and in the soma, and failure to degrade short-lived cargos, such as NSG2.

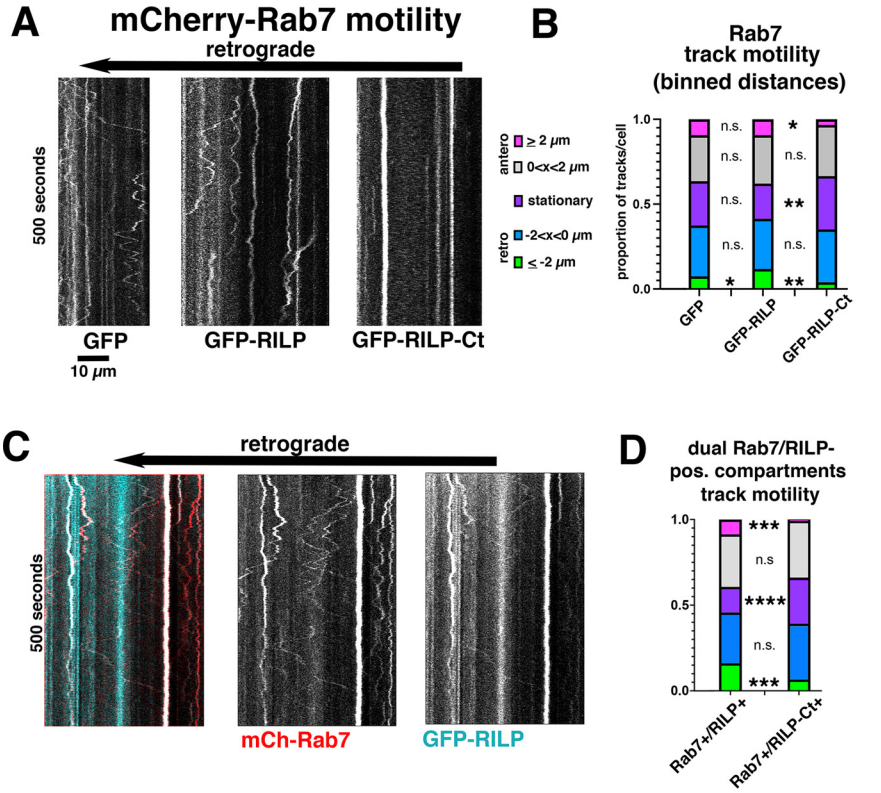

E

Directional motility of Rab7 compartments
(based on graphs in B and D)

Transfection	retrograde (all) +	anterograde (all) +	SEM	Stat Signif.
mCh-Rab7 +GFP	51% (Rab7-pos)	49% (Rab7-pos)	2%	n.s.
mCh-Rab7+GFP-RILP	52% (Rab7-pos)	48% (Rab7-pos)	3%	n.s.
dual Rab7+/RILP+	53% (dual positive)	47% (dual positive)	3%	*
	(>2μm)	(>2μm)		
mCh-Rab7 +GFP	44% (Rab7-pos)	56% (Rab7-pos)	7%	n.s.
mCh-Rab7+GFP-RILP	59% (Rab7-pos)	41% (Rab7-pos)	5%	**
dual Rab7+/RILP+	62% (dual positive)	38% (dual positive)	5%	****

Figure 6. Motility of dendritic LEs is affected by overexpression of WT RILP or RILP-Ct. ***A***, ***B***, Live imaging of mCherry-Rab7 in neurons transfected with GFP, GFP-RILP, or GFP-RILP-Ct. ***A***, Examples of kymographs of mCherry-Rab7 motility in dendrites (soma on the left). ***B***, Quantification of mcherry-Rab7 net motility for GFP controls, GFP-RILP, or GFP-RIL-Ct-expressing neurons. Net distances of trajectories for each cell were binned as indicated. Net distances for all motile tracks are plotted in Extended Data Figure 6-1. N = 21-27 neurons from three independent experiments (76-110 dendrites). $^{*}p < 0.05$; $^{**}p < 0.01$; Kruskal–Wallis or one-way ANOVA test (as appropriate for nonparametric or parametric dataset). ***C***, ***D***, Motility of dual Rab7/RILP-positive endosomes based on experiments from ***A***, ***B***. ***C***, Example of kymographs of mCherry-Rab7 (middle) and GFP-RILP (right) motility. ***D***, Quantification of net motility for compartments dually positive for mcherry-Rab7 and GFP-RILP (binned by net distance per cell). Net distances for all motile tracks are plotted in Extended Data Figure 5-1. N = 20-22 cells, three independent experiments. $^{****}p < 0.0001$; $^{***}p < 0.001$; Kruskal–Wallis test. ***E***, Directional bias of compartments based on graphs in ***B***, ***D***. Green + blue bars represent Retrograde All. Pink + gray bars represent Anterograde All. Green bars represent Retrograde ≥ 2 μm. Pink bars represent Anterograde ≥ 2 μm.

Dynein promotes long-range, bidirectional motility of LEs in dendrites

In order to more directly test roles for dynein in LE motility in dendrites, we overexpressed the dynein/dynactin inhibitor GFP-CC1 (Fig. 9*A*,*B*; Extended Data Fig. 9-1) and conducted the same analysis as for RILP-Ct in Figures 6 and 8. Inhibition of dynein with GFP-CC1 greatly reduced motility of Rab7 bidirectionally (Fig. 9*B*). In addition, we used ciliobrevin treatment (Roossien et al., 2015) for 2 h to acutely inhibit dynein function (Fig. 9*C*,*D*; Extended Data Fig. 9-1). The acute effects of ciliobrevin phenocopied GFP-CC1 expression: long-range bidirectional motility (pink and green bars) was inhibited, leading to an increase in the stationary population (Fig. 9*D*, purple bar). The short-range motility populations (gray and blue bars) were less consistently affected and appear overall less sensitive to dynein inhibition (Fig. 9*D*). Net distances traveled are shown in Extended Data Figure 9-1.

We also tested the dynein sensitivity of NSG1 compartment motility by live imaging (Fig. 9*E*–*H*; Extended Data Fig. 9-1). We observed inhibition of long-range bidirectional motility in GFP-CC1 transfected dendrites (Fig. 9*E*,*F*), similar to what we observed for Rab7 (Fig. 9*A*,*B*). Acute inhibition of dynein with

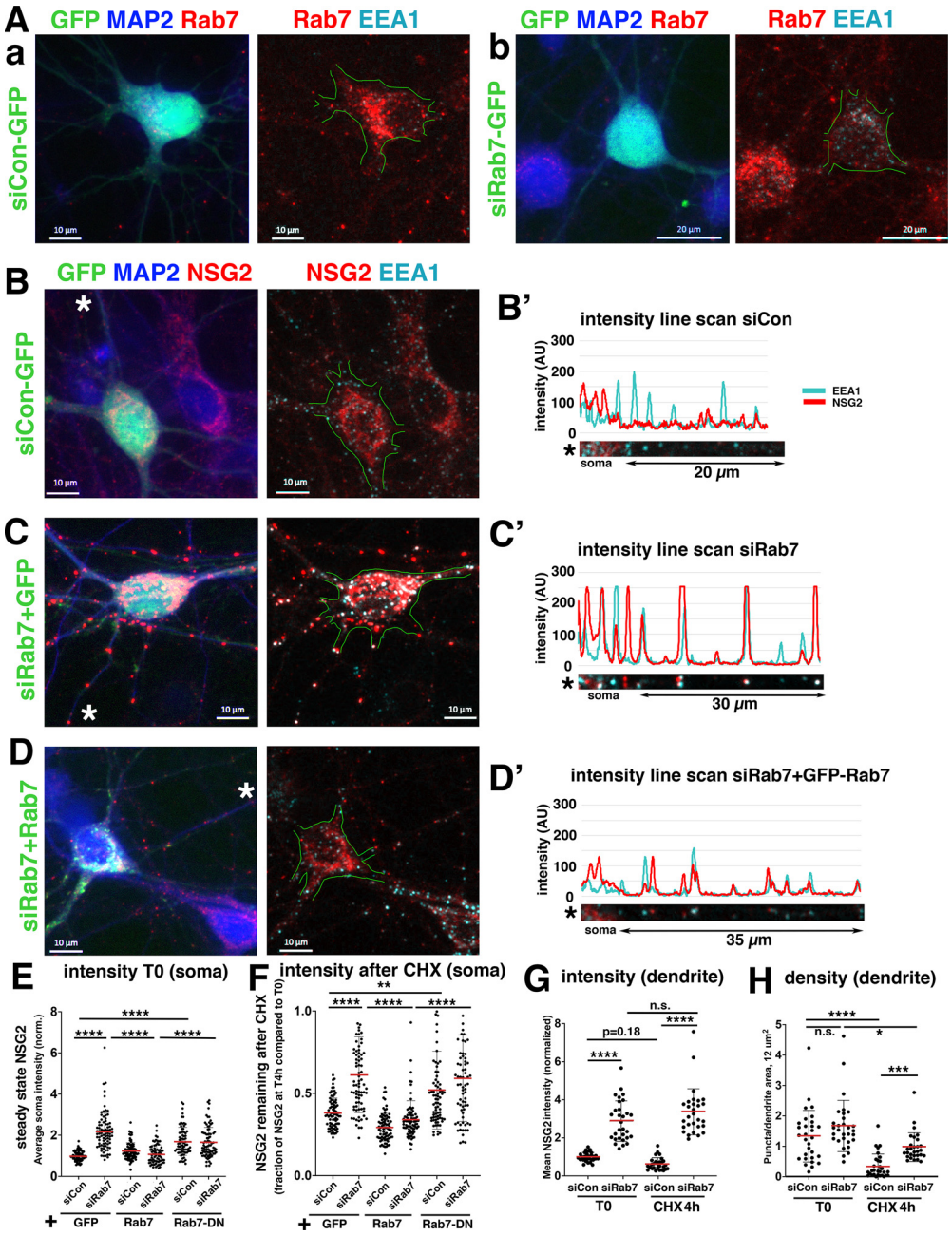

Figure 7. siRab7 delays degradation of the short-lived dendritic cargo NSG2. ***A***, Knockdown efficiency of siRab7. Neurons were transfected with siControl (***Aa***) or siRab7 (***Ab***) together with GFP at DIV5 and incubated for 6 d and then immunostained against Rab7 (red) and EEA1 (cyan). MAP2 (blue) staining identifies dendrites. Transfected neurons are outlined in green. Quantification of knockdown efficiency is shown in Extended Data Figure 7-1. ***B-D***, Immunostaining against NSG2 (red) and EEA1 (cyan) in neurons transfected with siControl (***B***) or siRab7 together with GFP (***C***) or siRab7 together with GFP-Rab7 (***D***; "rescue") for 6 d. MAP2 (blue) staining identifies dendrites. Transfected neurons are outlined in green. White asterisks indicate the dendrites shown in ***B′-D′***. ***B′-D′***, Line scans along dendrites marked with asterisks in ***B-D*** are shown to illustrate the increased NSG2 and EEA1 signal in siRab7. ***E-H***, Quantifications of NSG2 signal intensity and density in neurons transfected with siControl or siRab7. GFP, GFP-Rab7, or GFP-Rab7DN were cotransfected with siRNA for 6 d. Cultures were fixed and stained either at steady state (T0) (***E***) or treated with CHX for 4 h (***F***). ***E***, At steady state, knockdown of Rab7 significantly increased NSG2 in somatic endosomes. This phenotype was rescued by overexpression of GFP-Rab7 but not of GFP-Rab7DN. $N = 67$-80 neurons, three independent experiments. $^{****}p < 0.0001$; $^{**}p < 0.01$; Kruskal–Wallis test. ***F***, Retention of NSG2 in the soma after 4 h CHX treatment (retention normalized to steady-state T0) is plotted as a measure of degradation. Downregulation of Rab7 with siRab7 significantly impaired degradation of NSG2. Degradation was rescued by coexpression of GFP-Rab7 but not of GFP-Rab7DN. $N = 67$-80 neurons, three independent experiments. $^{****}p < 0.0001$; $^{**}p < 0.01$; $^{*}p < 0.05$; Kruskal–Wallis test. ***G***, ***H***, NSG2 intensity (***G***) and density (***H***) of dendritic endosomes were determined for siCon and siRab7 at steady state (T0) and after 4 h CHX (T4). $N = 30$-32 neurons, three independent experiments. $^{****}p < 0.0001$. $^{***}p < 0.001$. $^{*}p < 0.05$. All error bars are standard deviations.

ciliobrevin (Fig. 9*G*,*H*) also significantly decreased the bidirectional motility of NSG1-mCh compartments. Our data indicate that dynein supports long range anterograde and retrograde transport of LEs in dendrites but has little effect on local short range net motility.

We additionally overexpressed the dynein intermediate chain GFP-DIC2C in the hopes of evaluating the motility of compartments that had recruited dynein. GFP-DIC2C had a substantial cytosolic pool which made observations of labeled compartments not possible. We thus assessed the mobility of total mCh-Rab7 (Fig. 9*A*,*B*) or NSG1-mCh (Fig. 9*E*,*F*) compartments in neurons overexpressing GFP-DIC2C to determine whether GFP-DIC2C overexpression affected their motility. Overexpressing GFP-DIC2C did not change

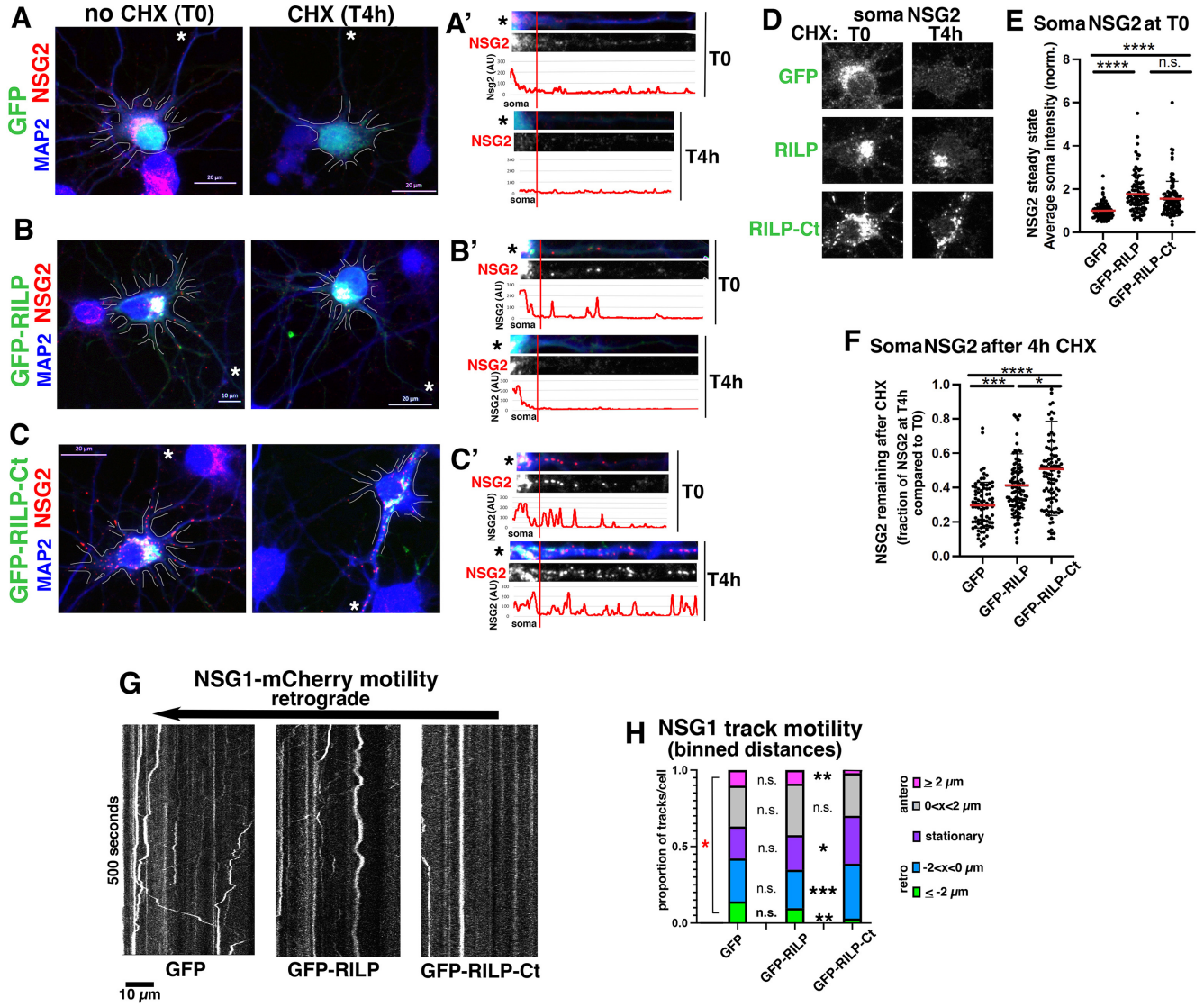

Figure 8. Preventing dynein recruitment to LEs leads to degradative delays. ***A-F***, DIV8 neurons were transfected with GFP (***A***), GFP-RILP (***B***) or GFP-RILP-Ct (***C***) and stained against endogenous NSG2 at steady state (T0; left) or after 4 h CHX (T4h; right). ***A-C***, The transfected neuron is outlined in white. Dendrites marked with white asterisks in ***A-C*** are shown in ***A′-C′*** with corresponding NSG2 intensity line scans, as labeled. ***D***, The red channel (NSG2) is shown alone for the soma region of the transfected cell for easier comparison of NSG2 accumulation caused by RILP and RILP-Ct overexpression. In RILP overexpression, NSG2 accumulated exclusively in the soma at T4h (compare with dendrite scan in ***B′***), whereas overexpression of RILP-Ct accumulated NSG2 in the soma and along dendrites (compare with dendrite scan in ***C′***). ***E***, ***F***, Quantification of soma fluorescence intensity of NSG2 in transfected neurons at steady-state T0 (***E***) or remaining after 4 h CHX (***F***). Overexpression of GFP-RILP-Ct overexpression led to inhibition of NSG2 degradation, and GFP-RILP partially impaired degradation compared with the control. ***E***, $N = 87$-104 neurons, from three independent cultures. $^{****}p < 0.0001$ (Kruskal–Wallis test). ***F***, $N = 82$-100 neurons, three independent experiments. $^{****}p < 0.0001$; $^{***}p < 0.001$; $^{*}p < 0.05$; Kruskal–Wallis test. All error bars are standard deviations. ***G***, ***H***, Live imaging of NSG1-mCherry in neurons cotransfected with GFP, GFP-RILP, or GFP-RILP-Ct. Examples of kymographs of NSG1-mCherry motility (***G***) (soma on the left). ***H***, Net distances of trajectories for each cell were binned as indicated. Net distances for all motile tracks are plotted in Extended Data Figure 8-1. $N = 18$-27 neurons (77-114 dendrites) in three independent experiments. $^{****}p < 0.0001$; $^{**}p < 0.01$; $^{*}p < 0.05$; Kruskal–Wallis test or one-way ANOVA (as appropriate for nonparametric or parametric dataset). Red star indicates statistical comparison between pink and green bins for GFP condition. $^{*}p < 0.05$.

the proportion of motile compartments of mCh-Rab7 (Fig. 9*A*,*B*; Extended Data Fig. 9-1). Interestingly, overexpression of GFP-DIC2C decreased the proportion of stationary NSG1-mCh compartments (Fig. 9*F*, purple bar; Extended Data Fig. 9-1) and significantly increased anterograde long-range motility of NSG1-mCh compartments (Fig. 9*F*). Again, short-range net motility compartments (gray and blue bars) were not changed (Fig. 9*F*).

We then wondered whether degradative lysosomes were motile and dynein-regulated. We loaded neurons with the degradation sensor DQ-BSA (Marwaha and Sharma, 2017; Yap et al., 2018) and conducted live imaging after 18 h of chase. Motility of DQ-BSA degradative compartments was extremely low in control dendrites (GFP; Fig. 9*I*; Extended Data Fig. 9-1) and was not further reduced by CC1. Interestingly, expression of GFP-DIC2C decreased the stationary population and significantly increased anterograde motility (Fig. 9*I*). Overall, the number of moving DQ-BSA compartments was very low under all conditions, compared with the motility observed for mCh-Rab7 or NSG1-mCh. Dynein adaptors other than RILP might account for some of the differences we observe between the behaviors of Rab7 and NSG1 or DQ-BSA.

Inhibition of dynein slows the degradation of dendritic cargos and affects dendrite length

Our current model of dendritic degradative flux posits that dendritic LEs need to move to the soma for terminal degradation

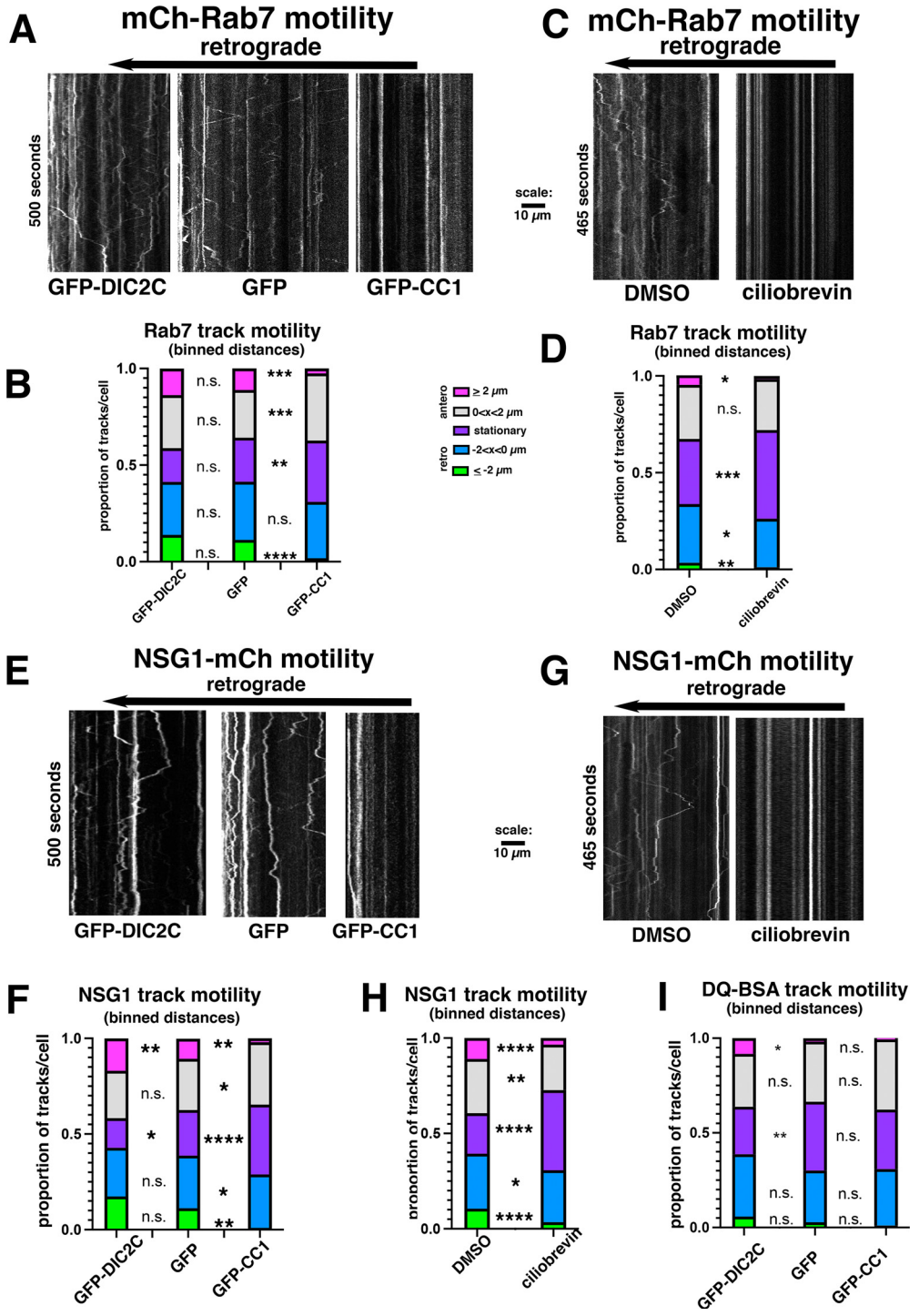

Figure 9. Dynein promotes long-range, bidirectional motility of Rab7 and degradative cargos in dendrites. ***A***, ***B***, Live imaging of mCherry-rab7 in neurons cotransfected with GFP, GFP-DIC2C, or GFP-CC1. ***A***, Examples of kymographs of mCherry-Rab7 motility (soma on the left). ***B***, Net distances of trajectories for each cell were binned as indicated. Net distances for all motile tracks are plotted in Extended Data Figure 9-1. Overexpression of GFP-CC1 significantly reduced the track travel distance of mCherry-Rab7 both retrogradely and anterogradely. N = 23-29 neurons (81-109 dendrites) from three independent experiments. $^{****}p < 0.0001$; $^{***}p < 0.001$; $^{**}p < 0.01$; Kruskal–Wallis test. ***C***, ***D***, Live imaging of mCherry-Rab7 in neurons treated with ciliobrevin D or DMSO control. ***C***, Examples of kymographs of mCherry-Rab7 motility. ***D***, Net distances of trajectories for each cell were binned as indicated. Net distances for all motile tracks are plotted in Extended Data Figure 8-1. Treatment with ciliobrevin D significantly reduced the movement of mCherry-Rab7 both retrogradely and anterogradely. N = 27-30 neurons (117-131 dendrites) from three independent experiments. $^{***}p < 0.001$; $^{**}p < 0.01$; $^{*}p < 0.05$; test, Mann–Whitney U or Student's t tests (as appropriate for nonparametric or parametric dataset). ***E***, ***F***, Live imaging of NSG1-mCherry in neurons coexpressing GFP, GFP-DIC2C, or GFP-CC1. ***E***, Examples of kymographs of NSG1-mCherry motility (soma on the left) and quantification in ***F***. Overexpression of GFP-CC1 significantly reduced the movement of NSG1-mCherry both retrogradely and anterogradely. N = 110-124 dendrites from 29-31 neurons, three independent experiments. $^{****}p < 0.0001$; $^{**}p < 0.01$; $^{*}p < 0.05$; Kruskal–Wallis test. ***G***, ***H***, Live imaging of NSG1-mCherry in neurons treated with DMSO or ciliobrevin D. Examples of kymographs of NSG1-mCherry motility in ***G***, and quantification in ***H***. Net distances for all motile tracks are plotted in Extended Data Figure 9-1. Treatment with ciliobrevin D significantly reduced the movement of NSG1-mCherry both retrogradely and anterogradely. N= 26-29 neurons (121-129 dendrites) from three independent experiments. $^{****}p < 0.0001$; $^{**}p < 0.01$; $^{*}p < 0.05$; Mann–Whitney U test. ***I***, Quantification of motility of DQ-BSA labeled compartments (presumptive lysosomes) in neurons transfected with GFP, or GFP-DIC2C, or GFP-CC1. N = 15-21 neurons (51-71 dendrites) from two independent experiments. $^{**}p < 0.01$; $^{*}p < 0.05$; Kruskal–Wallis or one-way ANOVA test (as appropriate for nonparametric or parametric dataset).

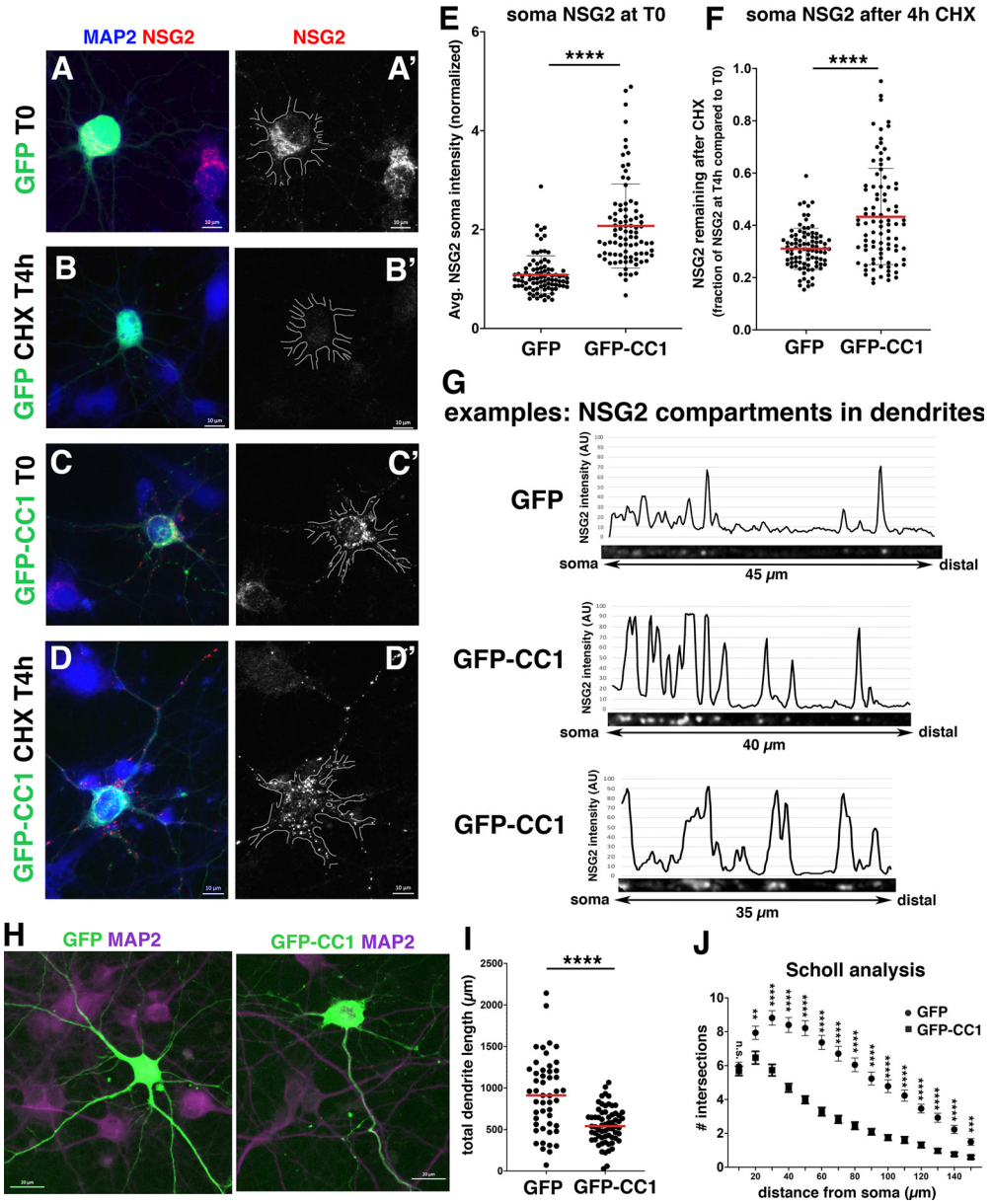

Figure 10. Inhibition of dynein slows the degradation of dendritic cargos and affects dendrite length. ***A-D***, DIV8 neurons were transfected with either GFP (***A***,***B***) or GFP-CC1 (***C***,***D***) and fixed at steady state (T0; ***A***,***C***) or treated with CHX for 4 h (T4h; ***B***,***D***) and stained against endogenous NSG2 (red; shown as single gray channel in ***A′-D′***). Transfected neurons are outlined in white. ***E***, ***F***, Quantification of soma fluorescence intensity of NSG2 in neurons transfected with either GFP or GFP-CC1 at steady-state T0 (***E***) or after 4 h CHX (***F***; NSG2 remaining after 4 h CHX). Overexpression of GFP-CC1 resulted in accumulation of NSG2 in the soma at steady-state T0 (***E***) and impaired degradation of NSG2 after 4 h CHX (***F***). ***E***, $N = 84$-87 neurons, three independent experiments. ****$p < 0.0001$ (Kruskal–Wallis test). ***F***, $N = 85$-91 neurons, three independent experiments. ****$p < 0.0001$ (Kruskal–Wallis test). ***G***, Examples of steady-state NSG2 distribution in dendrites of neurons transfected with GFP (top) or GFP-CC1 (middle and bottom) with line scans depicting the intensity and density of NSG2. Overexpression of GFP-CC1 led to accumulation of NSG2 compartments along dendrites. ***H-J***, Dendrite morphology of neurons expressing GFP (left) or GFP-CC1 (right) (***H***). MAP2 is used to designate dendrites. Quantification of total dendrite length (***I***) and Scholl analysis (no. of intersections with distance) (***J***) for neurons transfected with GFP or GFP-CC1. $N = 49$-65 neurons, three independent experiments. ****$p < 0.0001$ (Kruskal–Wallis test). All error bars are standard deviation.

(Yap et al., 2018). Since we observed inhibition of LE motility by GFP-CC1 and ciliobrevin, we next determined whether degradation of NSG2 was diminished by dynein inhibition using the CHX chase assay. Neurons were transfected with GFP as control (Fig. 10*A*,*B*) or GFP-CC1 (Fig. 10*C*,*D*), fixed at steady state (T0) (Fig. 10*A*,*C*) or incubated for 4 h in CHX (T4h) (Fig. 10*B*,*D*). NSG2 levels declined greatly after 4 h of CHX in GFP controls but were significantly increased at both T0 and T4h in CHX in GFP-CC1-expressing neurons (Fig. 10*A′-D′*,*E*,*F*). The observed degradation impairment was qualitatively similar to what we observed with siRab7 and RILP-Ct, but the degradation inhibition appeared less complete. NSG2 also accumulated in clustered/enlarged endosomes along dendrites (Fig. 10*G*). These observations reveal that efficient degradation of dendritic cargos (e.g., NSG2) requires functional dynein motor activity. Since degradative cargo accumulates in enlarged/clustered endosomes along dendrites, we surmise that the lack of degradation is because of lack of retrograde transport of dendritic endosomes to the soma.

During these experiments, we noticed that neuronal morphology seemed to be affected by GFP-CC1 expression. We thus determined the length of dendrites in GFP-expressing

control neurons and GFP-CC1-expressing neurons (Fig. 10*H*). Quantification of total length of dendritic processes (Fig. 10*I*) and Scholl analysis of dendrite complexity (Fig. 10*J*) revealed significantly decreased total dendrite length and complexity after 36 h of GFP-CC1 overexpression. The number of primary dendrites was not reduced (Fig. 10*J*, 10 µm distance), but dendrites branched less and were shorter. This effect could be because of lack of dendritic transport, lack of degradation, or both.

Dynein inhibition inhibits LE maturation in addition to LE transport

In many of our experiments, we observed that Rab7 levels were increased by our interference conditions (e.g., RILP-Ct in Fig. 2*D*). Excessive accumulation of Rab7 indicates that compartment progression which requires normal Rab7 cycling to advance LE maturation might be impaired, not just motility per se. We thus wondered whether the maturation of EEs or LEs was changed in any of our interference conditions. During the maturation of endosomes, EEs initially accumulate increasing levels of EEA1 but are Rab7-negative. Maturation of LEs depends on Rab7 recruitment to the EEA1-positive endosomes, changes in phosphoinositide composition, and ultimately dissociation of EEA1 to create a mature $Rab7^+/EEA1^-$ LE (Fig. 12*A*). Rab7 GDP/GTP cycling is required for proper maturation of EEs to LEs and for LE maturation (Vanlandingham and Ceresa, 2009; Girard et al., 2014). We therefore determined the levels of Rab7 in neurons expressing GFP-CC1 (Fig. 11*A–C*), as an indicator of LE maturation defects (increased Rab7; Fig. 11*B*,*C*). GFP-CC1 expression led to enlarged and brighter Rab7 compartments in the soma (Fig. 11*A*), but total Rab7 intensity in the soma was not increased (not shown). Since cytosolic Rab7 fluorescence appeared decreased, we quantified compartment-recruited Rab7 levels. This analysis revealed that dynein inhibition with GFP-CC1 increased the intensity of Rab7 recruited onto somatic endosomes (Fig. 11*B*) as well as their numbers (Fig. 11*C*). Inhibiting dynein thus interferes with normal progression of LE maturation as evidenced by abnormal accumulation of membrane-associated Rab7 on somatic endosomes.

Similar to GFP-CC1 overexpression, RILP-Ct or WT RILP overexpression also led to accumulated Rab7 in the soma (see also Fig. 2*C*,*D*). Rab7 was ~5-fold brighter in dendritic endosomes when RILP-Ct was overexpressed (Fig. 11*D*), indicating profound disruption of Rab7 cycling off endosomal membranes. The increased Rab7 fluorescence intensity observed by immunofluorescence could be because of increased retention of activated Rab7 on endosomes or because of increased Rab7 protein levels, or both. We thus prepared whole-cell lysates from neuronal cultures transfected with GFP, GFP-RILP, or GFP-RILP-Ct and blotted for endogenous Rab7 (Fig. 11*E*). Quantification of three experiments showed 1.5- to 2-fold increases in Rab7 signal (Fig. 11*E′*), indicating that the total Rab7 protein levels were elevated. Given that transfection efficiencies are only ~20% in the cultures, we estimate that the Rab7 levels in the RILP-Ct transfected neurons increased by 2.5- to 5-fold. Interestingly, we find that WT RILP overexpression also leads to increased Rab7 protein levels by Western blot (Fig. 11*E*,*E′*). These data suggest that over-recruitment of membrane-bound Rab7 by WT RILP is detrimental and impedes maturation events downstream of Rab7/RILP. Since overexpression of WT RILP impairs degradation of NSG2 in the soma (Fig. 8), but not motility of LEs in dendrites (Fig. 6), the maturation defect observed is a possible culprit for the degradation defects in WT-RILP-overexpressing neurons (see also Discussion).

Next, we determined whether EE-to-LE maturation was affected by determining EEA1 intensities. In agreement with findings in other cell types (Girard et al., 2014; Takahashi et al., 2017), we see increased levels of EEA1 in siRab7-treated neurons which were rescued by re-expression of WT Rab7 (Fig. 11*F*). EEA1 intensity, on the other hand, was unaffected when GFP-CC1 was expressed to inhibit dynein (Fig. 11*A*,*G*). Interestingly, we observed changes in EEs in RILP-CT-expressing neurons (Fig. 11*H*). EEA1 levels on dendritic endosomes were increased, albeit not as much as Rab7 levels (compare Fig. 11*D–H*). We also determined EEA1 and Rab7 intensity on the $EEA1^+/Rab7^+$ dually positive transitioning EE-LE endosomes (see diagram in Fig. 12*A*) and found a modest increase in EEA1 intensity (Fig. 11*I*) and a large increase in Rab7 intensity (Fig. 11*J*) also on these maturing endosomes. The percentage of colocalization of EEA1 compartments with Rab7 or of Rab7 compartments with EEA1 was not changed significantly and remained between 15% and 20% colocalization in RILP-Ct-overexpressing dendrites, similar to controls (not shown). In summary, our results unexpectedly show a significant increase in total Rab7 associated with endosomes when either dynein was inhibited or an effector with impaired dynein function was overexpressed, raising the possibility of novel roles for dynein in endosome maturation. In addition, we observe that endosome maturation is also changed by the overexpression of WT RILP, raising interesting questions about the coordination of maturation and Rab7 effector progression.

Discussion

Our previous work identified a process that requires directional retrograde transport in dendrites (Yap et al., 2018), namely, the efficient degradation of short-lived membrane proteins, such as NSG1/2. We found that the bulk of degradation takes place in or near the soma where lysosomes are greatly enriched. In addition, retrograde degradative flux in dendrites was inhibited by dominant-negative Rab7, the master regulator of LEs (Yap et al., 2018). Here we ask which microtubule motor is responsible for Rab7-dependent retrograde transport of dendritic LEs to the soma for degradation. We used both dynein inhibition and promotion/inhibition of dynein recruitment to LEs to show: (1) Degradation of dendritic cargos requires dynein. (2) Dynein/dynactin is required for net retrograde transport of LEs to the soma. (3) Disturbing dynein recruitment to LEs changes EE-LE maturation. Merely moving LEs to the soma is not sufficient for promoting degradation. Over-recruitment of membrane-bound Rab7 impedes maturation events downstream of Rab7/RILP and leads to failed degradation. Last, live imaging reveals that recruiting dynein to LEs via RILP can increase the proportion of retrograde movements, raising future questions about the mechanisms by which directional transport in dendrites is enhanced. In conclusion, Rab7 is required for maturation of dendritic endosomes and for recruitment of dynein motors to support net dendritic retrograde transport to lysosomes. We propose that interference with dynein recruitment to dendritic endosomes or with dynein function results in maturation defects, transport defects, and degradation impairment. Our model (Fig. 12) is discussed below.

Dynein motor is required for net retrograde movements of LEs to the soma

How directional transport in dendrites is achieved has been a long-standing puzzle because of the mixed polarity microtubule array with

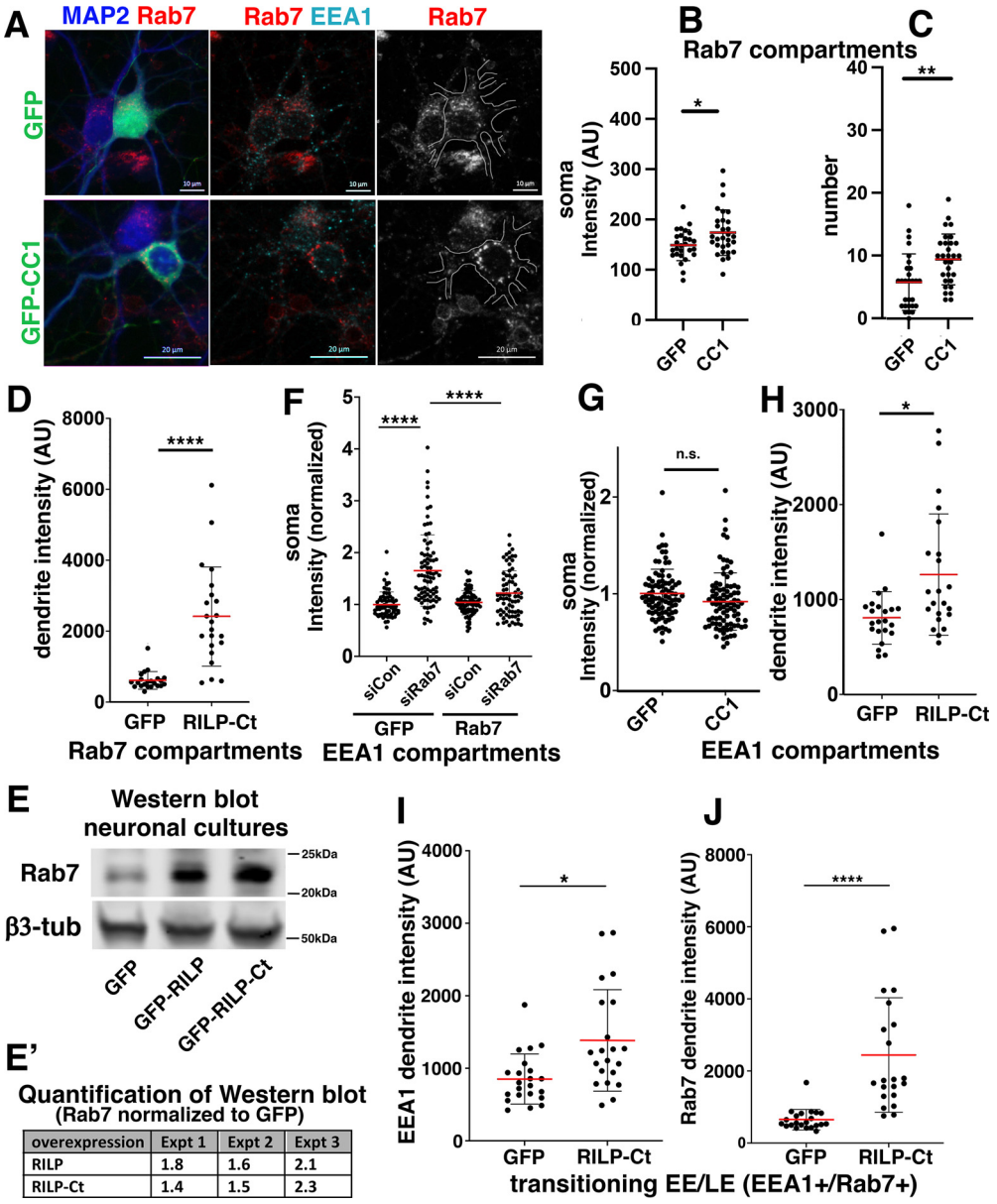

overexpression	Expt 1	Expt 2	Expt 3
RILP	1.8	1.6	2.1
RILP-Ct	1.4	1.5	2.3

Figure 11. Effects of dynein inhibition on maturation of late endosomes. ***A-C***, DIV8 neurons were transfected with either GFP or GFP-CC1 and stained against endogenous Rab7 and EEA1 (***A***). Transfected neuron is outlined in white. Gray represents single channels of Rab7. ***B***, ***C***, Quantification of soma fluorescence of Rab7 on somatic endosomes (apparent size >2 μm). Overexpression of GFP-CC1 significantly increased somatic Rab7 intensity (***B***) as well as the numbers of those endosomes (***C***). $N=30$ neurons, three independent experiments. $^{**}p<0.01$; $^{*}p<0.05$; Mann–Whitney *U* or Student *t* test. EEA1 intensities were quantified from the same cells and plotted separately as EEA1 compartments below (***G***). ***D***, ***E***, ***G-J***, DIV8 neurons were transfected with either GFP or GFP-RILP-Ct and stained against endogenous Rab7 and EEA1. Rab7 and EEA1 intensities were quantified from the same cells and plotted separately as EEA1 compartments (***H***), Rab7 compartments (***D***), and transitioning EE-LE compartments (***I***,***J***). ***E***, ***E′***, Western blot detection of Rab7 protein level in neurons nucleofected with GFP, GFP-RILP, or GFP-RILP-Ct. β3-tubulin was used to normalize loading. ***E′***, Quantification of Rab7 level by Western blot from three experiments. ***F***, Quantification of soma fluorescence intensity of EEA1 in neurons transfected with siRab7 or siControl, together with either GFP, or GFP-Rab7 ("rescue"). siRab7 significantly increased EEA1 signals in the soma, which could be rescued by coexpressing GFP-Rab7 in knockdown neurons. $N=67$-78 neurons, three independent experiments. $^{****}p<0.0001$ (Kruskal–Wallis test). ***G***, Overexpression of GFP-CC1 did not alter somatic endosomal EEA1 signals (***E***). These data correspond to the EEA1 channel shown in ***A***. $N=30$ neurons, three independent experiments. $^{**}p<0.01$; $^{*}p<0.05$; Mann–Whitney *U* or Student *t* test. ***D***, ***H***, Overexpression of GFP-RILP-Ct significantly increased both the somatic signals of Rab7 (***D***) and EEA1 (***H***) compared with the control, indicating possible delay in EE exit to LE. $N=20$-22 neurons, from two independent experiments, Kruskal–Wallis test. ***I***, ***J***, EEA1 intensity (***I***) and Rab7 intensity (***J***) on dendritic transitioning EE-LE compartments were quantified. Transitioning EE-LE compartments are dually positive for EEA1 and Rab7. $N=20$-22 neurons, two independent experiments. $^{****}p<0.0001$; $^{*}p<0.05$; Kruskal–Wallis test. All error bars are standard deviation.

only slight excess of plus-end out microtubules (~55%) (Kapitein and Hoogenraad, 2015; Masucci et al., 2021). Experimental recruitment of dynein motors to peroxisomes demonstrated unequivocally that dynein, in principle, supports bidirectional motility in dendrites (Kapitein et al., 2010; Ayloo et al., 2017). Accordingly, dynein is implicated in both retrograde and anterograde transport.

Our experiments examined endogenous endosome motility focusing on the master regulator of LEs (Rab7) and degradative cargos (NSG1/2). We show that dendritic LEs are driven retrogradely to the soma when dynein is recruited via RILP overexpression. Recruiting kinesin-1 to LEs via FYCO1 overexpression did not result in retrograde movement, indicating that dynein provides retrograde motor activity for dendritic LEs. Earlier work indicated that other organelles also use dynein in dendrites (Aiken and Holzbaur, 2021), but dynein-driven LE motility toward the soma was not previously described.

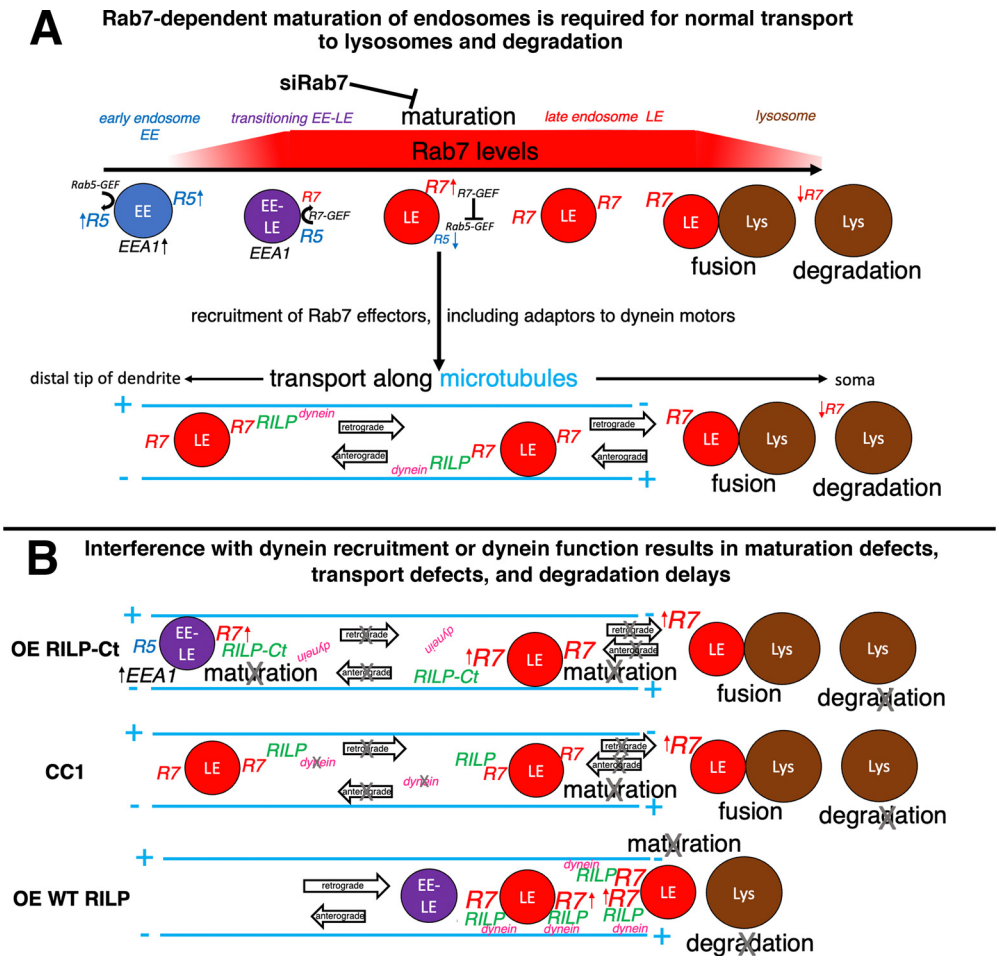

Figure 12. Model of dynein regulation in dendritic endosome maturation and transport. ***A***, Rab7-dependent maturation of endosomes is required for normal transport to lysosomes and degradation. EEs have high levels of Rab5 and EEA1. Rab7 is activated and recruited onto maturing LEs, giving rise to a transient double-positive EEA1/Rab7 transitioning EE/LE population. Increasing Rab7 activation leads to dissociation of Rab5 and EEA1, resulting in Rab7-positive LEs. Regulation of active Rab7-GTP is driven by Rab7-GEF, which also inactivates the Rab5-GEF. LEs recruit a multitude of Rab7 effectors, including motor adaptors for dynein, such as RILP. RILP-mediated dynein recruitment to LEs results in net retrograde transport to somatic lysosomes where fusion and degradation occur. Active Rab7 has been proposed to diminish on mature lysosomes. ***B***, Interference with dynein recruitment (overexpression: OE RILP-Ct) or dynein inactivation (CC1) leads to transport defects and degradation delays. Additionally, there is over-recruitment of active Rab7 on endosomes, suggesting that normal maturation is disrupted. Over-recruited Rab7-containing compartments trap RILP and are less competent to fuse with degradative lysosomes. Overexpression of WT RILP (OE WT RILP) promotes recruitment of dynein and increased retrograde transport of dendritic endosomes to the soma, but degradation of dendritic cargos is nevertheless impaired. This suggests a model in which OE WT RILP locks Rab7 in the activated, membrane-bound GTP state, which does not allow cycling of Rab7 to exchange RILP for other downstream Rab7 effectors, such as fusion machinery.

Our extensive live imaging shows that overall LE transport was bidirectional with many stationary phases and little retrograde bias at baseline. Some vesicles travel fairly processively toward the soma. Others travel toward the tip of the dendrite, and most remain more or less in place. Retrograde transport of LEs in dendrites is thus inefficient. Inhibition of dynein activity or of dynein recruitment inhibited both anterograde and retrograde motility. Careful analysis of directional bias in tracks revealed that the short-range tracks behaved differently than long-range (≥2 μm) tracks: Inhibition of dynein or of dynein recruitment increased stationary tracks, decreased long-range bidirectional motility, but not short-range motility. We surmise that short-range motility is largely independent of dynein. Instead, it might depend on myosins (van Bommel et al., 2019) or kinesins (Ghiretti et al., 2016; Masucci et al., 2021).

Net retrograde transport is increased by boosting dynein recruitment

Surprisingly, we uncovered increased retrograde transport bias with overexpression of RILP. This was particularly striking when LEs that had successfully recruited RILP (dually positive for Rab7 and RILP) were analyzed: we now see a statistically significant retrograde bias resulting in 62% retrograde tracks. Several of the better studied dynein adaptors, such as Bicaudal or Hook, activate dynein motors (Olenick and Holzbaur, 2019). Some also increase loading of dynein onto dynamic microtubule plus ends, thus increasing dynein-mediated motility (Jha et al., 2017; Lee et al., 2018; Canty and Yildiz, 2020). RILP, on the other hand, has not been shown to be an activating adaptor for dynein. How then can RILP increase retrograde motility? Processive motility requires that multiple motors work simultaneously (Jha and Surrey, 2015; Reck-Peterson et al., 2018). Estimates are that 6-12 dynein motors copurify with a 100-nm-sized lysosomes isolated from brain (Aiken and Holzbaur, 2021). We speculate that RILP overexpression increases dynein number on LEs, so that RILP stabilizes more active motors per endosome rather than activating inactive motors (see model in Fig. 12*B*). Vesicles undergoing longer directional transport events likely have a high number of active motors and might be walking along microtubules that are bundled with other microtubules of the same orientation. Such

microtubule bundles of "like" orientation have been detected in mammalian dendrites (Tas et al., 2017). The combination of large motor teams and "like" bundled tracks is predicted to result in increased processivity and would thus lead to more vesicles undergoing net long-range transport in dendrites. Our findings of increased retrograde bias of overexpressed RILP is consistent with the notion of some preference of "high-dynein" vesicles to associate with dynamic, tyrosinated, plus end-out microtubules which account for ~70% of microtubules (McKenney et al., 2016; Nirschl et al., 2016). How dynein is activated on LEs remains to be determined. Unexpectedly, overexpression of DIC decreased the stationary pool and slightly increased anterograde bias for NSG1 and DQ-BSA, but not for Rab7. This might reflect regulation by non-RILP dynein adaptors in transport of some of these vesicles. More work is needed to better understand this finding.

Degradation of dendritic short-lived cargos requires dynein recruitment to LEs and movement to the soma

Our previous observations (Yap et al., 2018) predicted that blocking retrograde transport would block efficient degradation. Consistent with this notion, inhibition of dynein recruitment by RILP-Ct or inhibition of dynein motor activity resulted in greatly reduced degradation of NSG2 (see model in Fig. 12*B*). NSG2 accumulated several-fold not only in somatic compartments, but also in many endosomes along dendrites. These dendritic compartments appeared larger and often clustered or arrayed in rows, like cars on a train. It is currently not certain what the clustered "train cars" tell us about the regions of dendrites where such apparent traffic jams occur, but there might be structural heterogeneities that cause the observed piling up of many compartments in discrete regions of the dendrite.

Overexpression of RILP impairs Rab7 cycling on LEs and blocks degradation

Our results clearly show that retrograde transport of LEs is required for degradation, but it is not sufficient. RILP overexpression resulted in clustered LE/Lys compartments in the soma which accumulated very high levels of Rab7 as well as of NSG2. NSG2 accumulation is analogous to the block of EGF degradation by RILP overexpression in fibroblasts (Wang and Hong, 2006). Consistent with our observations, RILP has been shown to lock Rab7 in its activated GTP-bound form on membranes (Jordens et al., 2001). Surprisingly, we observed an increase in total Rab7 levels in neurons, as well as increased $p150^{glued}$ recruitment. We did not see this in pilot experiments in NRK cells, and others have not seen increased total Rab7 levels in RILP-overexpressing fibroblasts (Jordens et al., 2001). Why the response to RILP overexpression is different in neurons than other cell types is an open question.

What does the increase in membrane-recruited Rab7 on degradation-blocked LEs tell us about endosomal progression to degradation? The molecular cascades that order and coordinate sequential steps in LE/lysosome progression are complex and not fully understood (Bonifacino and Neefjes, 2017; Marwaha et al., 2017). We propose that RILP locks Rab7-GTP on maturing dendritic LEs and prevents Rab7 cycling to exchange RILP/dynein for downstream effectors that are required for degradation (see model in Fig. 12*B*). A possible candidate is the fusion/tethering complex HOPS (Stroupe, 2018; van der Beek et al., 2019) which might require Rab7 cycling and exchange for dynein on RILP for fusion with co-clustered lysosomes. In addition, bound RILP might block some of the downstream effectors which deliver Rab7-GAPs to promote cycling of Rab7-GTP on LEs/lysosomes to promote progression (Jongsma et al., 2020). The profound disturbances in motility, degradation, and Rab7 cycling caused by increased WT RILP expression might explain why RILP is expressed at very low levels in neurons/brain and point to a delicate balancing of Rab7 activity and effector levels.

Surprisingly, we also find increased Rab7 associated with somatic endosomes when dynein is inhibited (see model Fig. 12*B*), suggesting an unanticipated role for dynein in endosome maturation.

Rab7 downregulation slows conversion of EEs to LEs. Similarly, RILP-Ct overexpression slowed conversion to EEA1-negative LEs. Rab7 levels were also greatly increased in RILP-Ct, again suggesting a disturbance of the normal orchestrated progression from EE to LE to lysosome when Rab7 cycling is impaired by misexpression of a single Rab7 effector (see model in Fig. 12*B*). In conclusion, interference with dynein recruitment to endosomes or with dynein function results in maturation defects, retrograde transport defects, and degradation delays of LEs/lysosomes. These findings might illuminate the molecular defects in human diseases associated with Rab7 (Cogli et al., 2009) and dynein/dynactin (Marzo et al., 2019).

References

Aiken J, Holzbaur EL (2021) Cytoskeletal regulation guides neuronal trafficking to effectively supply the synapse. Curr Biol 31:R633–R650.

Ayloo S, Guedes-Dias P, Ghiretti AE, Holzbaur EL (2017) Dynein efficiently navigates the dendritic cytoskeleton to drive the retrograde trafficking of BDNF/TrkB signaling endosomes. Mol Biol Cell 28:2543–2554.

Baas PW, Black MM, Banker GA (1989) Changes in microtubule polarity orientation during the development of hippocampal neurons in culture. J Cell Biol 109:3085–3094.

Bentley M, Decker H, Luisi J, Banker G (2015) A novel assay reveals preferential binding between Rabs, kinesins, and specific endosomal subpopulations. J Cell Biol 208:273–281.

Boecker CA, Olenick MA, Gallagher ER, Ward ME, Holzbaur EL (2020) ToolBox: live imaging of intracellular organelle transport in induced pluripotent stem cell-derived neurons. Traffic 21:138–155.

Bonifacino JS, Neefjes J (2017) Moving and positioning the endolysosomal system. Curr Opin Cell Biol 47:1–8.

Borchers AC, Langemeyer L, Ungermann C (2021) Who's in control? Principles of Rab GTPase activation in endolysosomal membrane trafficking and beyond. J. Cell Biol 220:e202105120.

Bucci C, Thomsen P, Nicoziani P, McCarthy J, van Deurs B (2000) Rab7: a key to lysosome biogenesis. Mol Biol Cell 11:467–480.

Cantalupo G, Alifano P, Roberti V, Bruni CB, Bucci C (2001) Rab-interacting lysosomal protein (RILP): the Rab7 effector required for transport to lysosomes. EMBO J 20:683–693.

Canty JT, Yildiz A (2020) Activation and regulation of cytoplasmic dynein. Trends Biochem Sci 45:440–453.

Cason SE, Carman PJ, Van Duyne C, Goldsmith J, Dominguez R, Holzbaur EL (2021) Sequential dynein effectors regulate axonal autophagosome motility in a maturation-dependent pathway. J Cell Biol 220:e202010179.

Choudhury A, Dominguez M, Puri V, Sharma DK, Narita K, Wheatley CL, Marks DL, Pagano RE (2002) Rab proteins mediate Golgi transport of caveola-internalized glycosphingolipids and correct lipid trafficking in Niemann-Pick C cells. J Clin Invest 109:1541–1550.

Cogli L, Piro F, Bucci C (2009) Rab7 and the CMT2B disease. Biochem Soc Trans 37:1027–1031.

Farfel-Becker T, Roney JC, Cheng XT, Li S, Cuddy SR, Sheng ZH (2020) The secret life of degradative lysosomes in axons: delivery from the soma, enzymatic activity, and local autophagic clearance. Autophagy 16:167–168.

Ferguson SM (2018) Axonal transport and maturation of lysosomes. Curr Opin Neurobiol 51:45–51.

Ghiretti AE, Thies E, Tokito MK, Lin T, Ostap EM, Kneussel M, Holzbaur EL (2016) Activity-dependent regulation of distinct transport and cytoskeletal remodeling functions of the dendritic kinesin KIF21B. Neuron 92:857–872.

Girard E, Chmiest D, Fournier N, Johannes L, Paul JL, Vedie B, Lamaze C (2014) Rab7 is functionally required for selective cargo sorting at the early endosome. Traffic 15:309–326.

Gowrishankar S, Lyons L, Rafiq NM, Roczniak-Ferguson A, De Camilli P, Ferguson SM (2021) Overlapping roles of JIP3 and JIP4 in promoting axonal transport of lysosomes in human iPSC-derived neurons. Mol Biol Cell 32:1094–1103.

Guerra F, Bucci C (2016) Multiple roles of the small GTPase Rab7. Cells 5:34.

Huotari J, Helenius A (2011) Endosome maturation. EMBO J 30:3481–3500.

Jakobs MA, Dimitracopoulos A, Franze K (2019) KymoButler, a deep learning software for automated kymograph analysis. Elife 8:e42288.

Jha R, Surrey T (2015) Regulation of processive motion and microtubule localization of cytoplasmic dynein. Biochem Soc Trans 43:48–57.

Jha R, Roostalu J, Cade NI, Trokter M, Surrey T (2017) Combinatorial regulation of the balance between dynein microtubule end accumulation and initiation of directed motility. EMBO J 36:3387–3404.

Jin EJ, Kiral FR, Hiesinger PR (2018a) The where, what, and when of membrane protein degradation in neurons. Dev Neurobiol 78:283–297.

Jin EJ, Kiral FR, Ozel MN, Burchardt LS, Osterland M, Epstein D, Wolfenberg H, Prohaska S, Hiesinger PR (2018b) Live observation of two parallel membrane degradation pathways at axon terminals. Curr Biol 28:1027–1038.e4.

Johansson M, Rocha N, Zwart W, Jordens I, Janssen L, Kuijl C, Olkkonen VM, Neefjes J (2007) Activation of endosomal dynein motors by stepwise assembly of Rab7-RILP-p150Glued, ORP1L, and the receptor betalll spectrin. J Cell Biol 176:459–471.

Jongsma ML, Bakker J, Cabukusta B, Liv N, van Elsland D, Fermie J, Akkermans JL, Kuijl C, van der Zanden SY, Janssen L, Hoogzaad D, van der Kant R, Wijdeven RH, Klumperman J, Berlin I, Neefjes J (2020) SKIP-HOPS recruits TBC1D15 for a Rab7-to-Arl8b identity switch to control late endosome transport. EMBO J 39:e102301.

Jordens I, Fernandez-Borja M, Marsman M, Dusseljee S, Janssen L, Calafat J, Janssen H, Wubbolts R, Neefjes J (2001) The Rab7 effector protein RILP controls lysosomal transport by inducing the recruitment of dynein-dynactin motors. Curr Biol 11:1680–1685.

Kapitein LC, Hoogenraad CC (2015) Building the neuronal microtubule cytoskeleton. Neuron 87:492–506.

Kapitein LC, Schlager MA, Kuijpers M, Wulf PS, van Spronsen M, MacKintosh FC, Hoogenraad CC (2010) Mixed microtubules steer dynein-driven cargo transport into dendrites. Curr Biol 20:290–299.

Khobrekar NV, Quintremil S, Dantas TJ, Vallee RB (2020) The dynein adaptor RILP controls neuronal autophagosome biogenesis, transport, and clearance. Dev Cell 53:141–153.

Klumperman J, Raposo G (2014) The complex ultrastructure of the endolysosomal system. Cold Spring Harb Perspect Biol 6:a016857.

Kulkarni VV, Maday S (2018) Compartment-specific dynamics and functions of autophagy in neurons. Dev Neurobiol 78:298–310.

Langemeyer L, Fröhlich F, Ungermann C (2018) Rab GTPase function in endosome and lysosome biogenesis. Trends Cell Biol 28:957–970.

Lasiecka ZM, Winckler B (2011) Mechanisms of polarized membrane trafficking in neurons: focusing in on endosomes. Mol Cell Neurosci 48:278–287.

Lasiecka ZM, Yap CC, Caplan S, Winckler B (2010) Neuronal early endosomes require EHD1 for L1/NgCAM trafficking. J Neurosci 30:16485–16497.

Lasiecka ZM, Yap CC, Katz J, Winckler B (2014) Maturational conversion of dendritic early endosomes and their roles in L1-mediated axon growth. J Neurosci 34:14633–14643.

Lee IG, Olenick MA, Boczkowska M, Franzini-Armstrong C, Holzbaur EL, Dominguez R (2018) A conserved interaction of the dynein light intermediate chain with dynein-dynactin effectors necessary for processivity. Nat Commun 9:986.

Lie PP, Nixon RA (2019) Lysosome trafficking and signaling in health and neurodegenerative diseases. Neurobiol Dis 122:94–105.

Lin X, Yang T, Wang S, Wang Z, Yun Y, Sun L, Zhou Y, Xu X, Akazawa C, Hong W, Wang T (2014) RILP interacts with HOPS complex via VPS41 subunit to regulate endocytic trafficking. Sci Rep 4:7282.

Luzio JP, Parkinson MD, Gray SR, Bright NA (2009) The delivery of endocytosed cargo to lysosomes. Biochem Soc Trans 37:1019–1021.

Maday S, Holzbaur EL (2016) Compartment-specific regulation of autophagy in primary neurons. J Neurosci 36:5933–5945.

Marques AR, Saftig P (2019) Lysosomal storage disorders—challenges, concepts and avenues for therapy: beyond rare diseases. J Cell Sci 132: jcs221739.

Marwaha R, Arya SB, Jagga D, Kaur H, Tuli A, Sharma M (2017) The Rab7 effector PLEKHM1 binds Arl8b to promote cargo traffic to lysosomes. J Cell Biol 216:1051–1070.

Marwaha R, Sharma M (2017) DQ-red BSA trafficking assay in cultured cells to assess cargo delivery to lysosomes. Bio Protoc 7:e2571.

Marzo MG, Griswold JM, Ruff KM, Buchmeier RE, Fees CP, Markus SM (2019) Molecular basis for dyneinopathies reveals insight into dynein regulation and dysfunction. Elife 8:e47246.

Masucci EM, Relich PK, Lakadamyali M, Ostap EM, Holzbaur EL (2021) Microtubule dynamics influence the retrograde biased motility of kinesin-4 motor teams in neuronal dendrites. Mol Biol Cell mbcE21100480.

McKenney RJ, Huynh W, Vale RD, Sirajuddin M (2016) Tyrosination of α-tubulin controls the initiation of processive dynein-dynactin motility. EMBO J 35:1175–1185.

McMahon L, Digilio L, Duston A, Yap CC, Winckler B (2021) KymoMerge: a new tool for analysis of multichannel kymographs. BioRxiv. doi:10.1101/2021.11.29.470387.

Naslavsky N, Caplan S (2018) The enigmatic endosome: sorting the ins and outs of endocytic trafficking. J. Cell Sci 131:jcs216499.

Nirschl JJ, Magiera MM, Lazarus JE, Janke C, Holzbaur EL (2016) α-Tubulin tyrosination and CLIP-170 phosphorylation regulate the initiation of dynein-driven transport in neurons. Cell Rep 14:2637–2652.

Nixon RA, Yang DS (2011) Autophagy failure in Alzheimer's disease: locating the primary defect. Neurobiol Dis 43:38–45.

Olenick MA, Holzbaur EL (2019) Dynein activators and adaptors at a glance. J Cell Sci 132:jcs227132.

Pankiv S, Alemu EA, Brech A, Bruun JA, Lamark T, Overvatn A, Bjørkøy G, Johansen T (2010) FYCO1 is a Rab7 effector that binds to LC3 and PI3P to mediate microtubule plus end-directed vesicle transport. J Cell Biol 188:253–269.

Parenti G, Medina DL, Ballabio A (2021) The rapidly evolving view of lysosomal storage diseases. EMBO Mol Med 13:e12836.

Peng W, Minakaki G, Nguyen M, Krainc D (2019) Preserving lysosomal function in the aging brain: insights from neurodegeneration. Neurotherapeutics 16:611–634.

Progida C, Malerød L, Stuffers S, Brech A, Bucci C, Stenmark H (2007) RILP is required for the proper morphology and function of late endosomes. J Cell Sci 120:3729–3737.

Quintyne NJ, Gill SR, Eckley DM, Crego CL, Compton DA, Schroer TA (1999) Dynactin is required for microtubule anchoring at centrosomes. J Cell Biol 147:321–334.

Reck-Peterson SL, Redwine WB, Vale RD, Carter AP (2018) The cytoplasmic dynein transport machinery and its many cargoes. Nat Rev Mol Cell Biol 19:382–398.

Roossien DH, Miller KE, Gallo G (2015) Ciliobrevins as tools for studying dynein motor function. Front Cell Neurosci 9:252.

Schwenk BM, Lang CM, Hogl S, Tahirovic S, Orozco D, Rentzsch K, Lichtenthaler SF, Hoogenraad CC, Capell A, Haass C, Edbauer D (2014) The FTLD risk factor TMEM106B and MAP6 control dendritic trafficking of lysosomes. EMBO J 33:450–467.

Scott CC, Vacca F, Gruenberg J (2014) Endosome maturation, transport and functions. Semin Cell Dev Biol 31:2–10.

Stavoe AK, Holzbaur EL (2019) Autophagy in neurons. Annu Rev Cell Dev Biol 35:477–500.

Stroupe C (2018) This is the end: regulation of Rab7 nucleotide binding in endolysosomal trafficking and autophagy. Front Cell Dev Biol 6:129.

Sun J, Deghmane AE, Bucci C, Hmama Z (2009) Detection of activated Rab7 GTPase with an immobilized RILP probe. Methods Mol Biol 531:57–69.

Takahashi K, Mashima H, Miura K, Maeda D, Goto A, Goto T, Sun-Wada GH, Wada Y, Ohnishi H (2017) Disruption of small GTPase Rab7 exacerbates the severity of acute pancreatitis in experimental mouse models. Sci Rep 7:2817.

Tan SC, Scherer J, Vallee RB (2011) Recruitment of dynein to late endosomes and lysosomes through light intermediate chains. Mol Biol Cell 22:467–477.

Tanabe H, et al. (2018) Clinical and genetic features of Charcot-Marie-Tooth disease 2F and hereditary motor neuropathy 2B in Japan. J Peripher Nerv Syst 23:40–48.

Tas RP, Chazeau A, Cloin BM, Lambers ML, Hoogenraad CC, Kapitein LC (2017) Differentiation between oppositely oriented microtubules controls polarized neuronal transport. Neuron 96:1264–1271.

Vallee RB, Yi J, Quintremil S, Khobrekar N (2021) Roles of the multivalent dynein adaptors BicD2 and RILP in neurons. Neurosci Lett 752:135796.

van Bommel B, Konietzny A, Kobler O, Bär J, Mikhaylova M (2019) F-actin patches associated with glutamatergic synapses control positioning of dendritic lysosomes. EMBO J 38:e101183.

van der Beek J, Jonker C, van der Welle R, Liv N, Klumperman J (2019) CORVET, CHEVI and HOPS: multisubunit tethers of the endo-lysosomal system in health and disease. J Cell Sci 132:jcs189134.

Vanlandingham PA, Ceresa BP (2009) Rab7 regulates late endocytic trafficking downstream of multivesicular body biogenesis and cargo sequestration. J Biol Chem 284:12110–12124.

Vitelli R, Santillo M, Lattero D, Chiariello M, Bifulco M, Bruni CB, Bucci C (1997) Role of the small GTPase Rab7 in the late endocytic pathway. J Biol Chem 272:4391–4397.

Wang T, Hong W (2002) Interorganellar regulation of lysosome positioning by the Golgi apparatus through Rab34 interaction with Rab-interacting lysosomal protein. Mol Biol Cell 13:4317–4332.

Wang T, Hong W (2006) RILP interacts with VPS22 and VPS36 of ESCRT-II and regulates their membrane recruitment. Biochem Biophys Res Commun 350:413–423.

Wang T, Ming Z, Xiaochun W, Hong W (2011) Rab7: role of its protein interaction cascades in endo-lysosomal traffic. Cell Signal 23:516–521.

Winckler B, Faundez V, Maday S, Cai Q, Guimas Almeida C, Zhang H (2018) The endolysosomal system and proteostasis: from development to degeneration. J Neurosci 38:9364–9374.

Wu M, Wang T, Loh E, Hong W, Song H (2005) Structural basis for recruitment of RILP by small GTPase Rab7. EMBO J 24:1491–1501.

Yap CC, Winckler B (2022) Spatial regulation of endosomes in growing dendrites. Dev Biol 486:5–14.

Yap CC, Vakulenko M, Kruczek K, Motamedi B, Digilio L, Liu JS, Winckler B (2012) Doublecortin (DCX) mediates endocytosis of neurofascin independently of microtubule binding. J Neurosci 32:7439–7453.

Yap CC, Digilio L, McMahon L, Winckler B (2017) The endosomal neuronal proteins Nsg1/NEEP21 and Nsg2/P19 are itinerant, not resident proteins of dendritic endosomes. Sci Rep 7:10481.

Yap CC, Digilio L, McMahon LP, Garcia AD, Winckler B (2018) Degradation of dendritic cargos requires Rab7-dependent transport to somatic lysosomes. J Cell Biol 217:3141–3159.

Yau KW, Schätzle P, Tortosa E, Pagès S, Holtmaat A, Kapitein LC, Hoogenraad CC (2016) Dendrites in vitro and in vivo contain microtubules of opposite polarity and axon formation correlates with uniform plus-end-out microtubule orientation. J Neurosci 36:1071–1085.

Ye M, Lehigh KM, Ginty DD (2018) Multivesicular bodies mediate long-range retrograde NGF-TrkA signaling. Elife 7:e33012.